Journal of Fluids and Structures 105 (2021) 103332

Contents lists available at ScienceDirect

Journal of Fluids and Structures

journal homepage: www.elsevier.com/locate/jfs

Numerical simulations of flow-induced vibrations of two rigidly coupled cylinders with uneven diameters in the upper transition Reynolds number regime

Clarissa Pires Vieira Serta, Marek Jan Janocha *, Guang Yin, Muk Chen Ong

Department of Mechanical and Structural Engineering and Materials Science, University of Stavanger, Stavanger, Norway

ARTICLE INFO

Article history:
Received 6 August 2020
Received in revised form 4 June 2021
Accepted 21 June 2021
Available online 9 July 2021

Keywords:
Flow-induced vibrations
Coupled cylinders
Turbulent flow
Wake pattern

ABSTRACT

Two degree-of-freedom (2-DoF) flow-induced vibrations (FIV) of two rigidly coupled cylinders are numerically investigated at the Reynolds number of 3.6×10^6. Two-dimensional (2D) Unsteady Reynolds-Averaged Navier–Stokes (URANS) simulations are performed combined with the $k-\omega$ SST turbulence model. A low mass-damping system is considered with a mass ratio of 2 and a damping ratio of zero. The diameter ratio is set to 0.25. The influence of the reduced velocity (U_r), the position angle (α) of the small cylinder relative to the large cylinder and the gap ratio (G/D) between the cylinders on the FIV response of the system are analyzed. The simulations are performed for $2 \leq U_r \leq 12$. To analyze the effect of α, three values are considered, [$\alpha = 0°$, 90°, 180°] with a constant value of $G/D = 0.1$. The effect of G/D is studied for the $\alpha = 90°$ configuration in which the $G/D = 0.25$ and $G/D = 0.5$ configurations are analyzed in addition to the $G/D = 0.1$ configuration. It is found that the lock-in regime extends beyond $U_r = 12$ for the $\alpha = 0°$, 180° and $\alpha = 90°$ at $G/D = 0.1$ and 0.25 configurations compared with the single cylinder configuration. Extended lock-in range is observed when the small cylinder is placed at $\alpha = 90°$, with $G/D = 0.1$, and at $\alpha = 180°$. In addition, for the $\alpha = 90°$ configuration, the results obtained for $\overline{C}_D$, $\overline{C}_L$ and $A_{y,max}/D$ converge to those of the single cylinder with the increase of G/D. A 2T shedding mode is observed for the single cylinder at $6.5 \leq U_r \leq 10$ and for the $\alpha = 0°$ configuration when $U_r \geq 8$. For the $\alpha = 90°$ and 180° configurations, the wake patterns are irregular. With the increase of G/D, a longer vortex street behind the small cylinder is observed, which creates many vortical structures in the wake of the cylinders.

© 2021 The Authors. Published by Elsevier Ltd. This is an open access article under the CC BY license (http://creativecommons.org/licenses/by/4.0/).

1. Introduction

Cylinder-type structures can be found in many engineering applications, such as in the design of offshore structures, heat exchangers, chimneys and cables, to name a few. In practice, they can often be installed in groups. Many complex phenomena can occur due to the interaction of the bodies with the surrounding fluid flow. An important example of fluid–structure interaction (FSI) is flow-induced vibrations (FIV). Vortex-induced vibration (VIV) is a subclass of FIV. The origin of VIV is the intermittent vortex shedding which leads to periodic body oscillations with limited amplitude. Another type of FIV is galloping, which unlike VIV, is caused by the fluctuations of the shear layers and is characterized by high displacement amplitudes. Placing one or more objects close to the main cylinder alters the dynamic response of the system

* Corresponding author.
E-mail address: marek.j.janocha@uis.no (M.J. Janocha).

https://doi.org/10.1016/j.jfluidstructs.2021.103332
0889-9746/© 2021 The Authors. Published by Elsevier Ltd. This is an open access article under the CC BY license (http://creativecommons.org/licenses/by/4.0/).

and the behavior of the hydrodynamic forces. Thus, it is of practical relevance to investigate the changes that occur in the flow when two cylinders with different diameters are placed in close proximity.

The work of Feng (1968) is among the earliest published experimental studies on VIV of elastically mounted cylinders. He investigated the one degree-of-freedom (1-DoF) VIV of a single cylinder and demonstrated the lock-in phenomenon. Kalghatgi and Sayer (1997) conducted experiments on piggyback pipelines at the Reynolds numbers between 9×10^4 and 3×10^5. They reported that the drag force is increased with the presence of the secondary pipe compared with that on a single cylinder. Besides, in the subcritical Reynolds number regime, the lift force points downward to the seabed, whereas in the critical Reynolds number regime, it points in the opposite direction. In the case of a single cylinder, the direction of the lift force is always towards the seabed for the studied flow regimes. Tsutsui et al. (1997) investigated the flow around two stationary coupled cylinders at Reynolds numbers in the order of $O(10^4)$. The diameter ratio d/D (where d is the diameter of the small cylinder) and the gap ratio G/D (where G is the distance between the cylinders) were kept constant at 0.45 and 0.06, respectively. The position angle α (defined as the angle between the horizontal plane and the line connecting the cylinders centers) was varied from 90° (cylinders are vertically aligned) to 180° (small cylinder downstream the large one). They noticed that when $\alpha \geq 150°$, the drag force on the main cylinder is lower compared to that on a single cylinder, and the lift force becomes zero. This was attributed to the presence of the small cylinder in the wake of the large one. Zang et al. (2012) conducted experiments using particle image velocimetry (PIV) to study vortex shedding and VIV of piggyback pipelines in the subcritical flow regime. Their results showed that the amplitude ratio A/D (where A denotes the vibration amplitude of the cylinder) is dependent on the gap ratio G/D. For G/D larger than 0.3, the amplitude resembles that of an isolated cylinder, so the influence of the small pipeline on the large one is small. In the work of Zang and Gao (2014), VIV response of piggyback pipelines was investigated using a hydro-elastic facility. Several configuration parameters were studied, such as α, d/D and G/D, and different Reynolds number values in the order of $O(10^4)$ were investigated. They found that VIV is suppressed significantly in the side-by-side configuration ($\alpha = 90°$) and when $G/D = 0.25$.

Numerical studies have also been conducted to study cylinders in various flow regimes. Regarding numerical simulations of FIV, Zhao and Yan (2013) investigated the two degree-of-freedom (2-DoF) VIV of two cylinders with different diameters in the low Reynolds number regime (Re = 250). They employed the Petrov–Galerkin Finite Element Method to solve the 2D URANS equations and the Arbitrary-Lagrangian–Eulerian approach to deal with the motion of the bodies. The main analyzed parameters were α and G/D for a low mass-damping system, in which the mass ratio m^* ($m^* = m/m_d$, where m and m_d are the mass of the cylinders and the displaced mass, respectively) was set to 2 and the damping ratio ζ ($\zeta = c/2\sqrt{km}$, c is the structural damping and k, the structural stiffness) was specified as zero. They reported that the lock-in range was increased for certain α values, such as 0° (small cylinder downstream the large one), 22.5°, 90° and 112.5°. Also, at $G/D = 0.2$, the vibration amplitude was reduced and the lock-in range was narrowed. In the work of Zhao et al. (2016), three-dimensional (3D) simulations were performed to analyze the VIV of two cylinders with different diameter and arranged side-by-side at Re = 1000. They applied similar numerical method as used by Zhao and Yan (2013). The values of m^* and ζ were kept at 2 and zero, respectively, and the reduced velocity U_r ($U_r = U_\infty/f_n D$, where f_n is the structural natural frequency) was varied from 2 to 15. Zhao et al. (2016) reported that the observed vortex shedding pattern was the 2S mode throughout the range of investigated U_r. Besides, at $U_r = 4$, the root-mean-square of the lift coefficient attained its maximum value and it was similar to that of a single cylinder. For U_r larger than 10, the drag and lift coefficients were not influenced by the increase of U_r. Studies by Han et al. (2018) and Kang et al. (2017) successfully reproduced the branching behavior reported by Jauvtis and Williamson (2004) confirming the ability of 2D URANS simulations to predict the response amplitudes and frequencies of VIV in the subcritical regime with reasonable accuracy. Furthermore, computations by Singh and Mittal (2005) suggested that the development of the shear layer vortices and their interactions with the boundary layer leading to its transition to a turbulent state is primarily a two-dimensional phenomenon. Wu et al. (2014) demonstrated that 2D URANS is capable of accurate predictions of VIV characteristics for the cylinder with turbulent boundary layer tripped by roughness strips.

In the present study, FIV with 2-DoF of two cylinders with uneven diameters at Re = 3.6×10^6 are investigated. The value of investigated Re is in the range of the upper transition Reynolds number regime, $1.5 \times 10^6 < \mathrm{Re} < 4 \times 10^6$ (Sumer and Fredsøe, 2006). The 2D flow around the two rigidly coupled cylinders is solved by using Unsteady Reynolds-Averaged Navier–Stokes equations (URANS) and the $k - \omega$ Shear Stress Transport (SST) turbulence model. The main objective is to study the effect of U_r and α on the FIV response of the system. Besides, for $\alpha = 90°$ configuration (a common configuration of piggyback pipelines) the effect of G/D is also investigated. Due to the complexity of such FSI, experimental and numerical studies are few. To the authors' knowledge, such investigations of two coupled cylinders in the upper transition regime have not been performed yet.

The outline of this paper is as follows. In Section 2, the governing equations of the flow and the numerical methods are described. The computational set-up, convergence and validation studies are presented in Section 3. In Section 4, FIV of two rigidly coupled cylinders is investigated, and the hydrodynamic force coefficients, vibration amplitudes, FFT analysis, motion trajectories and flow fields are discussed. Finally, the main findings are given in Section 5.

Table 1
Coefficient values in the $k-\omega$ SST turbulence model.

ϕ	σ_k	σ_ω	β^*	β	α
ϕ_1	0.85	0.5	0.09	0.075	0.555
ϕ_2	1	0.856	0.09	0.083	0.44

2. Governing equations and numerical methods

In the present study, the Reynolds-Averaged Navier–Stokes equations for an incompressible flow are the governing equations and can be written as:

$$\frac{\partial U_i}{\partial x_i} = 0, \tag{1}$$

$$\frac{\partial \mathrm{U}_i}{\partial t} + \mathrm{U_j}\frac{\partial \mathrm{U}_i}{\partial x_j} = -\frac{1\partial \mathrm{P}}{\rho \partial x_i} + \nu \frac{\partial^2 \mathrm{U}_i}{\partial {x_j}^2} - \frac{\partial(\overline{u_i' u_j'})}{\partial x_\mathrm{j}}, \tag{2}$$

where U_i ($i \in [1, 2]$) denotes the time averaged velocity components, u_i' ($i \in [1, 2]$) denotes the fluctuating part of velocity components, the fluid density is ρ, the time averaged pressure is P, and ν is the kinematic viscosity of the fluid.

The cylinders configurations investigated in the present study undergo FIV with 2-DoF. The two cylinders are rigidly coupled together and vibrate as a single rigid body. Moreover, they are modeled as one system elastically supported by dampers and springs. The equation of motion of the system is given as:

$$U_r^2 \frac{\partial^2 x_i}{\partial t^2} + 4\pi\zeta U_r \frac{\partial x_i}{\partial t} + 4\pi^2 x_i = \frac{2}{\pi}\frac{U_r^2 C_i}{m^*\left[1+(d/D)^2\right]} \tag{3}$$

where x_1 and x_2 are the displacements in the in-line and cross-flow directions, C_1 and C_2 (also denoted as C_D and C_L) are the corresponding force coefficients, drag and lift, d is the diameter of the small cylinder and D is the diameter of the large cylinder. The expression for the force coefficients, drag and lift, is given as:

$$C_i = \frac{1}{\frac{1}{2}\rho U_\infty^2 A}\int_\Gamma \left[\left(-P\boldsymbol{I} + \mu\left(\nabla \boldsymbol{u} + (\nabla \boldsymbol{u})^T\right)\right)\cdot \boldsymbol{n}\right]\cdot \boldsymbol{n_i} d\Gamma \tag{4}$$

where A is the coupled cylinders projected area, Γ denotes the coupled cylinders surface area, $\boldsymbol{I}$ is the identity tensor and μ is the dynamic viscosity of the fluid.

The $k-\omega$ SST model (Menter et al., 2003) is employed in the present study. The $k-\omega$ SST model is well implemented in OpenFOAM and has been successfully used and validated in many previously published studies such as Porteous et al. (2015), Nieto et al. (2015), Pang et al. (2016) and Janocha and Ong (2020). It combines the $k-\omega$ and the $k-\epsilon$ models. In far field regions of the flow, the $k-\epsilon$ is activated whereas $k-\omega$ is applied in wall proximity regions. The expressions for the turbulent kinetic energy k and the specific dissipation rate ω are written as:

$$\frac{Dk}{Dt} = \tilde{P}_k - \beta^* k\omega + \frac{\partial}{\partial x_i}\left[(\nu + \sigma_k \nu_t)\frac{\partial k}{\partial x_i}\right] \tag{5}$$

$$\tilde{P}_k = min\left[\nu_t \frac{\partial u_i}{\partial x_j}\left(\frac{\partial u_i}{\partial x_j} + \frac{\partial u_j}{\partial x_i}\right), 10\beta^* k\omega\right] \tag{6}$$

$$\frac{D\omega}{Dt} = \alpha S^2 - \beta\omega^2 + \frac{\partial}{\partial x_i}\left[(\nu + \sigma_\omega \nu_t)\frac{\partial \omega}{\partial x_i}\right] + 2(1-F_1)\frac{\sigma_{\omega 2}}{\omega}\frac{\partial k}{\partial x_i}\frac{\partial \omega}{\partial x_i} \tag{7}$$

where S is the strain rate invariant, the model coefficients are defined in Table 1 and the expression for the turbulent viscosity ν_t is given as:

$$\nu_t = \frac{a_1 k}{max\left(a_1\omega, SF_2\right)} \tag{8}$$

where $a_1 = 0.31$. The constant ϕ and the blending functions F_1 and F_2 are defined as:

$$\phi = F_1\phi_1 + (1-F_1)\phi_2 \tag{9}$$

$$F_1 = tanh\left\{\left\{min\left[max\left(\frac{\sqrt{k}}{\beta^*\omega y}, \frac{500\nu}{y^2\omega}\right), \frac{4k\sigma_{\omega 2}}{CD_{k\omega}y^2}\right]\right\}^4\right\} \tag{10}$$

$$F_2 = tanh\left\{\left[max\left(2\frac{\sqrt{k}}{\beta^*\omega y}, \frac{500\nu}{y^2\omega}\right)\right]^2\right\} \tag{11}$$

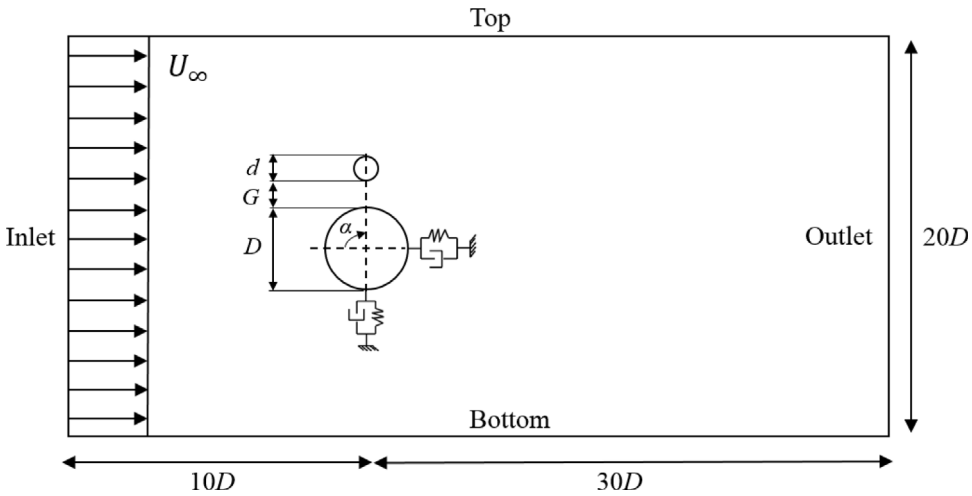

Fig. 1. Computational domain and boundary conditions.

Table 2
Domain size sensitivity study for the stationary single cylinder.

Mesh	Domain width	$\overline{C}_D$	$-C_{pB}$
W1	20D	0.480	0.553
W2	30D	0.479	0.553
W3	40D	0.479	0.552

where an expression for $CD_{k\omega}$ is given as:

$$CD_{k\omega} = max\left(2\sigma_{\omega 2}\frac{1}{\omega}\frac{\partial k}{\partial x_i}\frac{\partial \omega}{\partial x_i}, 10^{-10}\right) \tag{12}$$

The present simulations use the software OpenFOAM v1812. To solve the discretized equations of the flow, the PIMPLE algorithm is employed. It is a hybrid of the Semi-Implicit Method for Pressure-Linked Equations (SIMPLE) and the Pressure-Implicit with Splitting of Operators (PISO) algorithms. The second order Crank–Nicolson method is used for the time integration. The interpolation and Laplacian apply linear schemes and Gauss linear corrected, respectively. The schemes for divergence and gradient are Gauss linear.

3. Computational set-up, convergence and validation studies

3.1. Computational set-up

The computational domain employed in the present analyses is shown in Fig. 1. The domain is defined as a rectangular box with overall size of $40D \times 20D$. The upstream length is set as $10D$ from the inlet to the center of the large cylinder, and the downstream length is set as $30D$ from the center of the large cylinder to the outlet. In the cross-flow direction, the domain size extends $10D$ from the center of the large cylinder to the top and bottom boundaries, respectively. Ong et al. (2009) used a domain size of $27D \times 14D$ to conduct flow simulations at $\mathrm{Re} = 3.6 \times 10^6$ and reported that such distances to the boundaries show negligible influence on the flow in the vicinity of the body. Zhao et al. (2007) employed a domain of $28D \times 16D$ after a domain size investigation at $\mathrm{Re} = 4.1 \times 10^4$. Plakin et al. (2016) used domain width of $20D$ for simulations at $\mathrm{Re} = 1.4 \times 10^5$ and Rosetti et al. (2012) used a domain width of $20D$ for 2D URANS in a wide range of Re (up to $\mathrm{Re} = 5 \times 10^5$). To ensure that the blockage effect is not affecting the simulation results we conduct a domain width sensitivity study using three geometrically similar meshes (i.e. mesh in the central part is the same in each variant and meshes differ only by additional cell layers created at the top and bottom boundaries to obtain desired domain width). The results of the domain width sensitivity study summarized in Table 2 indicate that increasing the domain width from 20D to 30D and 40D has negligible influence on representative hydrodynamic quantities. Therefore, domain width of 20D appears to be sufficiently large to avoid the boundary proximity influence on the results in the present study.

The diameter ratio d/D is kept constant at $d/D = 0.25$ which is a typical value for offshore applications. Besides, a similar d/D was used in the previous works by Zhao et al. (2005), Zang et al. (2012, 2013). The gap between the cylinders is defined as G and the position angle of the small cylinder relative to the large cylinder is denoted as α, as shown in Fig. 1. The mesh morphing method used in the present study is based on spherical linear interpolation (SLERP). The motion of

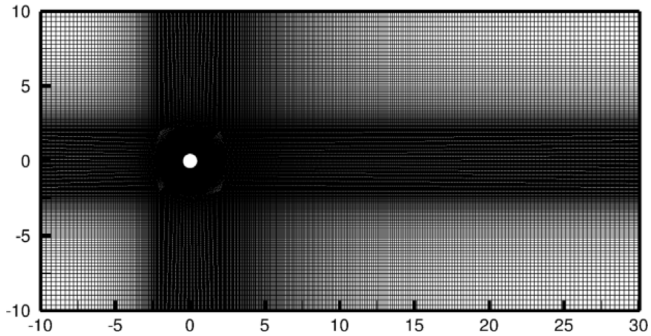

Fig. 2. Computational mesh for the single cylinder configuration: mesh A3 (Table 3).

the body is accommodated by morphing the computational mesh. Computational cells are moved according to the cosine profile in the predefined zone set between $0.5D$ and $7D$ normal to the moving boundary. The stiffness of the springs is the same in both the in-line and cross-flow directions $k_x = k_y$. Marine flowlines are typically lightly damped structures with low mass ratio, the properties selected in the present study are representative for such structures. The mass ratio is set as $m^* = 2$ and the damping ratio as $\zeta = 0$ for all the simulations. Thus, this low mass-damping system can reach large displacement amplitudes.

The imposed boundary conditions are given as follows:

1. Uniform flow with $u_x = U_\infty$ and $u_y = 0$ is prescribed at the inlet. The inlet values for k and ω are specified based on the following expressions:

$$k = \frac{3\,(U_\infty I)^2}{2} \tag{13}$$

$$\omega = \frac{\sqrt{k}}{l} \tag{14}$$

where the turbulence intensity I is set as 1% and the turbulent length scale l as D.

2. At the outlet, zero gradient condition is imposed for u_x, u_y, k and ω. The pressure P is set to zero.

3. On the cylinders walls, the no-slip condition is applied with $u_x = u_y = 0$. For k and ω, standard wall functions are specified as:

$$k = \frac{u_*^2}{\sqrt{C_\mu}} \tag{15}$$

$$\omega = \frac{\sqrt{k}}{\sqrt[4]{C_\mu}\,\kappa\, h_p} \tag{16}$$

where u_* denotes the friction velocity, the model constant is $C_\mu = 0.09$, the von Kármán constant is $\kappa = 0.41$ and h_p denotes the radial length between the cylinders surface and the center of the first cell adjacent to the cylinders surface.

4. At the top and bottom boundaries, zero normal gradient is prescribed for u_x, u_y, P, k and ω.

3.2. Convergence studies

The convergence studies are performed for a single cylinder and two coupled cylinders in the $\alpha = 90°$, $G/D = 0.1$ configuration. Firstly, a mesh dependence study is carried out for a stationary single cylinder. New simulations are then performed for a vibrating single cylinder using the same set of grid resolution from the simulations of the stationary cylinder. Time step convergence study is also carried out for the case with the vibrating single cylinder to find the maximum Courant number setting that minimizes time step errors. Secondly, a grid convergence study is carried out for two coupled cylinders in the $\alpha = 90°$, $G/D = 0.1$ configuration, and free to vibrate with 2-DoF.

Fig. 2 presents a complete view of a typical mesh used in the first stage of the convergence studies. The domain is composed of structured hexahedral elements. A high refinement is applied in the region around the cylinder and in the cylinder's wake. In the far field, the mesh is coarsened in order to reduce the computational cost. In Fig. 3, detailed views of the mesh around the cylinder are shown. The first cell height near the surface of the cylinder is set as $0.0005D$ which yields approximately averaged y^+ (here $y^+ = h_p u_*/\nu$) values in the range of 30 – 40. This value range is appropriate for the use of the specified wall functions.

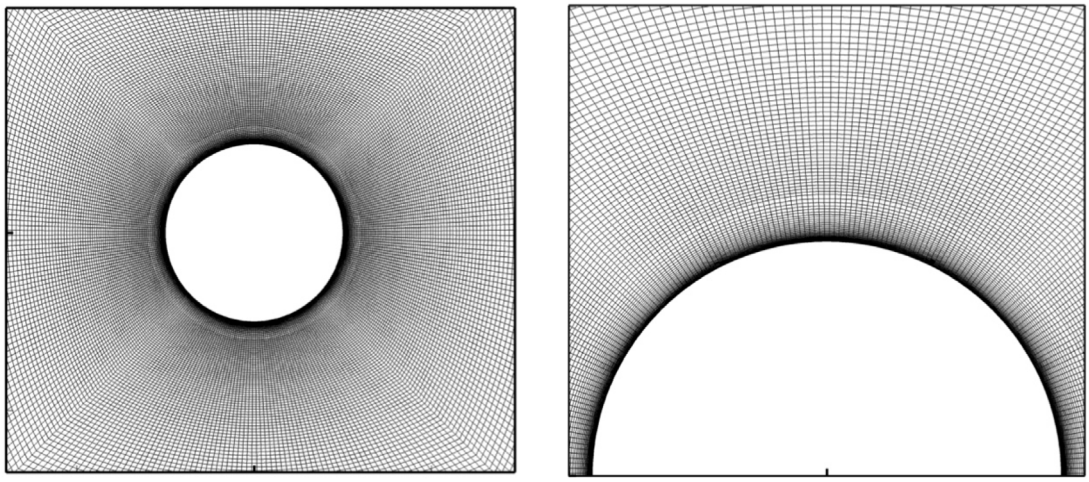

Fig. 3. Mesh details around the cylinder for the single cylinder configuration.

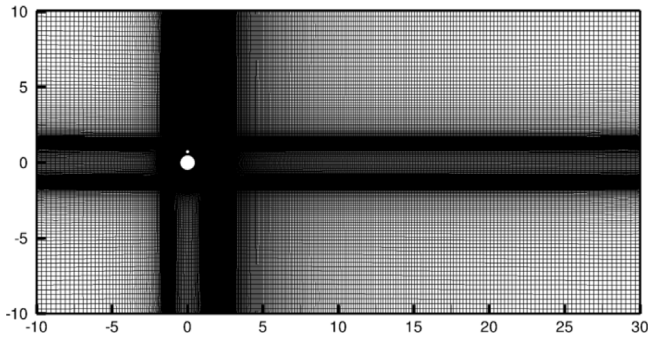

Fig. 4. Computational mesh for the two coupled cylinders configuration with $\alpha = 90^\circ$ and $G/D = 0.1$: mesh B3 (Table 6).

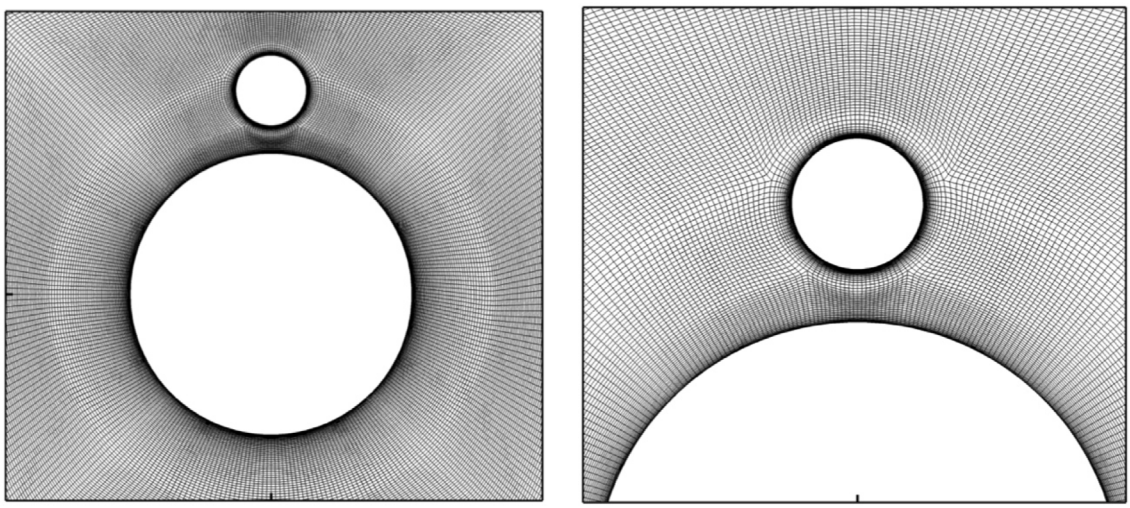

Fig. 5. Mesh details around the cylinders for the two coupled cylinder configuration with $\alpha = 90^\circ$ and $G/D = 0.1$.

Hydrodynamic force coefficients and the Strouhal number ($\mathrm{St} = fD/U_\infty$, here f is the vortex-shedding frequency) are used to evaluate the convergence. Expressions for the mean drag and mean lift coefficients are given as follows:

$$\overline{C}_D = \frac{1}{n}\sum_{i=1}^{n} C_{D,i} \tag{17}$$

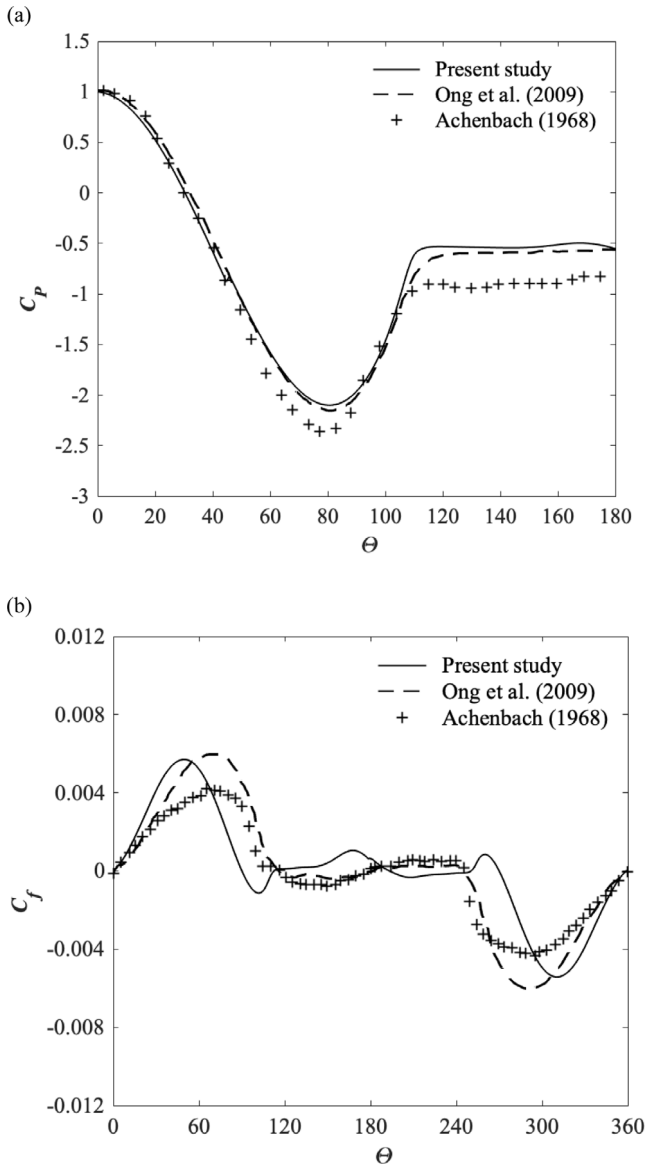

Fig. 6. Time-averaged pressure distribution (a) and skin friction distribution (b) around the single stationary cylinder at Re = 3.6×10^6.

$$\overline{C}_L = \frac{1}{n}\sum_{i=1}^{n} C_{L,i} \tag{18}$$

The corresponding root-mean-square values for the drag and lift coefficients are obtained by:

$$C_D^{rms} = \sqrt{\frac{1}{n}\sum_{i=1}^{n}\left(C_{D,i} - \overline{C}_D\right)^2} \tag{19}$$

$$C_L^{rms} = \sqrt{\frac{1}{n}\sum_{i=1}^{n}\left(C_{L,i} - \overline{C}_L\right)^2} \tag{20}$$

where n is the total number of time steps taken in the simulations.

In the grid resolution test for the stationary single cylinder case, four sets of meshes with an increment of approximately 40% in the total number of elements are assessed. A time step of $\Delta t = 0.002$ is employed in the simulations

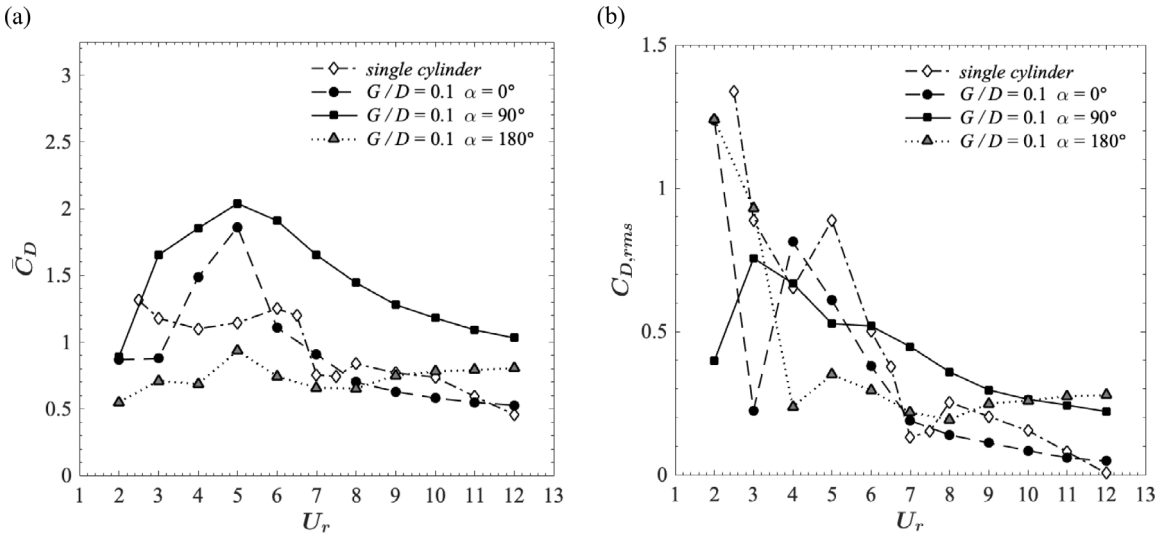

Fig. 7. Time-averaged drag coefficient $\overline{C}_D$ (a), root-mean-square of the drag coefficient $C_{D,rms}$ (b) for the single cylinder and $\alpha = [0°, 90°, 180°]$ configurations.

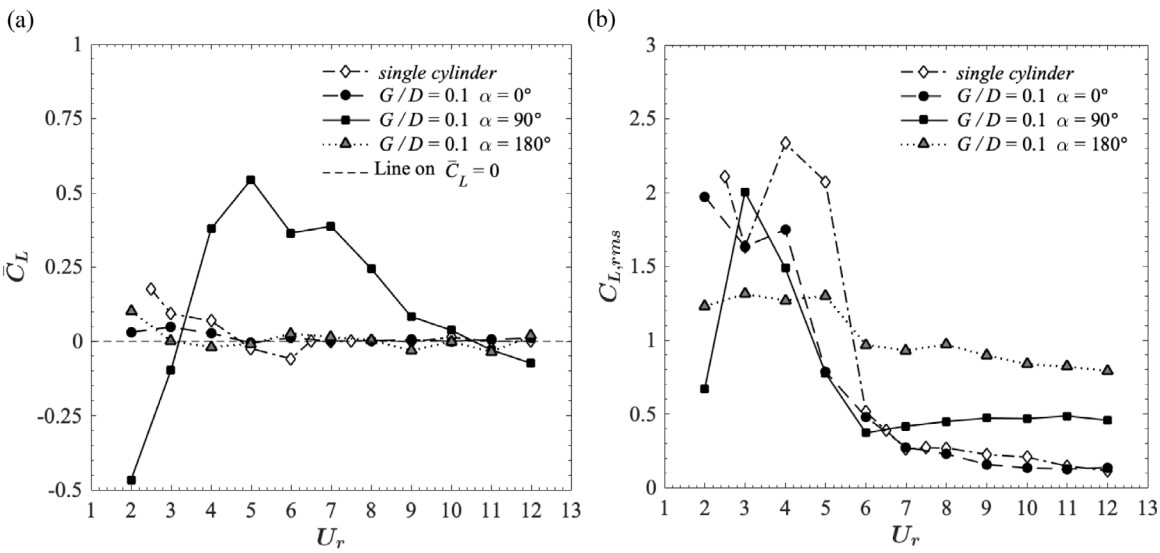

Fig. 8. Time-averaged lift coefficient $\overline{C}_L$ (a), root-mean-square of the lift coefficient $C_{L,rms}$ (b) for the single cylinder and $\alpha = [0°, 90°, 180°]$ configurations.

Table 3
Mesh convergence study for the stationary single cylinder.

Mesh	No. of cells	Time step	$\overline{C}_D$	$C_{L,rms}$	St
A1	53,595	$\Delta t = 0.002$	0.4492	0.153	0.3204
A2	74,889	$\Delta t = 0.002$	0.4547	0.162	0.3204
A3	1,04,536	$\Delta t = 0.002$	0.4616	0.175	0.3204
A4	1,46,092	$\Delta t = 0.002$	0.4625	0.174	0.3204

keeping the maximum Courant number below 0.60. The total non-dimensional duration of the simulations is set to $\tau = 200$ (here $\tau = tU_\infty/D$).

Table 3 summarizes the mesh parameters along with the corresponding results for the analyzed hydrodynamic quantities. The differences between the results obtained on the meshes A3 and A4 are smaller than 0.5% for $\overline{C}_D$, $C_{L,rms}$ and St.

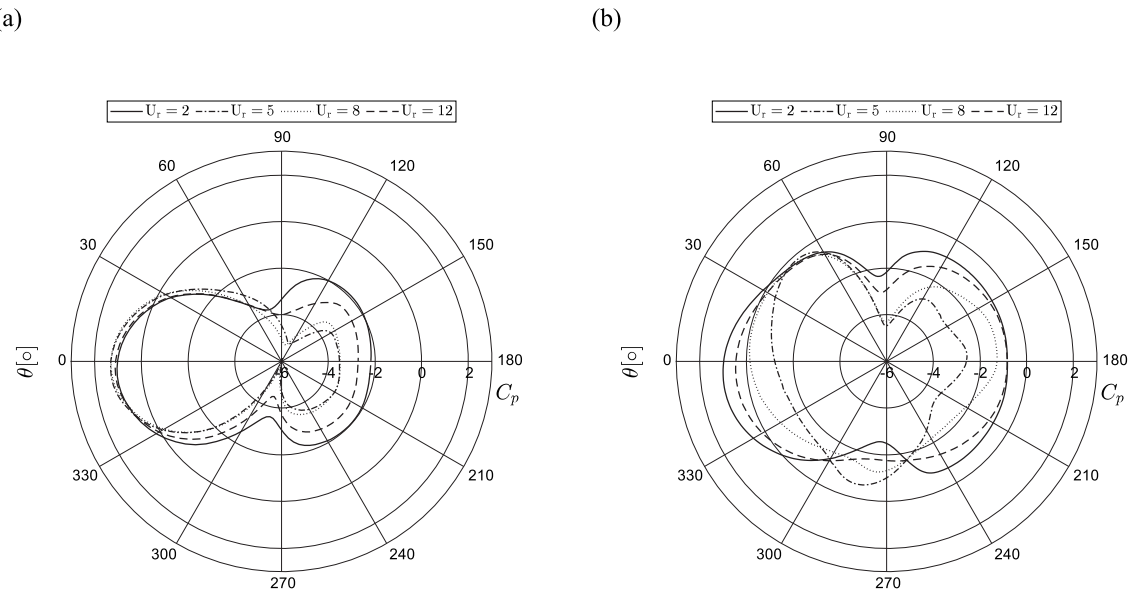

Fig. 9. Pressure coefficient distributions for the (a) small and (b) large cylinders for $G/D = 0.1$ and different U_r, $\alpha = 90°$ configuration.

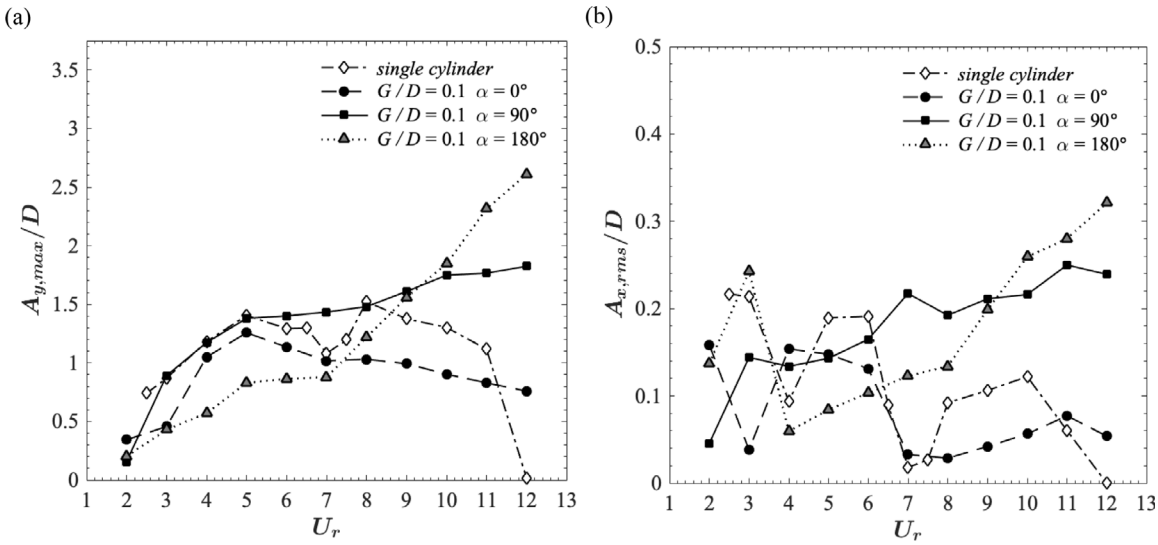

Fig. 10. Normalized maximum cross-flow vibration amplitude $A_{y,max}/D$ (a) and normalized root-mean-square of the in-line vibration amplitude $A_{x,rms}/D$ (b) for the single cylinder and $\alpha = [0°, 90°, 180°]$ configurations.

In the convergence study of the vibrating single cylinder, $U_r = 6$ is selected for the simulations where high in-line and transverse vibration amplitudes of the cylinder are expected. In the grid resolution analysis, the maximum Courant number is constrained to $Co_{max} = 0.5$. Besides the hydrodynamic force coefficients, displacement amplitudes are also used to compare the results obtained from the simulations with different grid resolutions. The normalized maximum vertical vibration amplitude is given by:

$$\frac{A_{y,max}}{D} = \frac{1}{2}\frac{\left|A_{y,max} - A_{y,min}\right|}{D} \tag{21}$$

The mesh settings along with the corresponding results for the analyzed parameters are given in Table 4. The relative differences in the calculated $\overline{C}_D$, $C_{L,rms}$ and St obtained using the meshes A3 and A4 are smaller than 1%. The relative difference in $A_{y,max}/D$ values between the simulations using the meshes A3 and A4 is 1.44%.

In the time step sensitivity analysis, three simulations with the mesh A3 (see Table 4) are carried out with different maximum Courant numbers of $Co_{max} = [0.25, 0.5, 1.0]$, and the obtained results are presented in Table 5. The relative

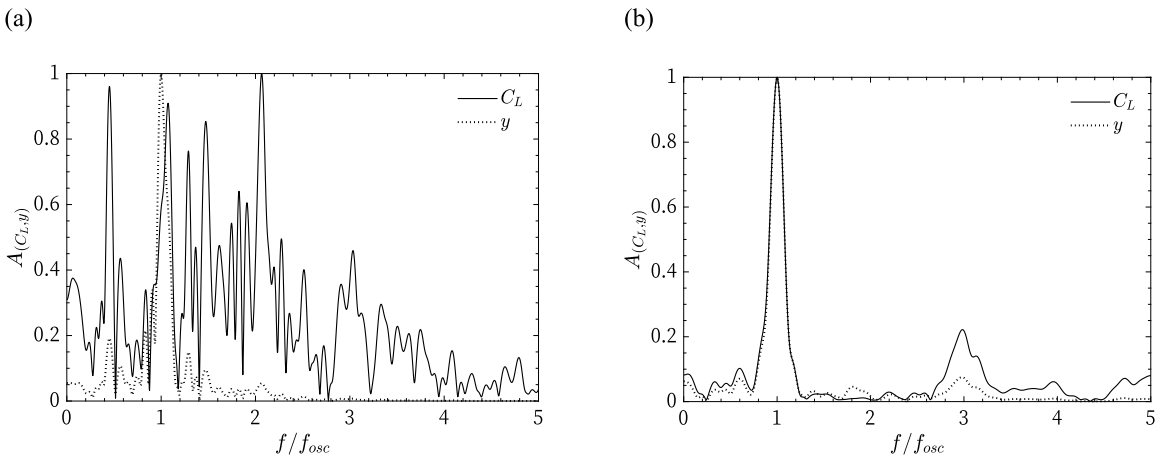

Fig. 11. FFT of the lift coefficient and cross-flow displacement time-series, (a) $\alpha = 90°$ configuration, (b) $\alpha = 180°$ configuration at $U_r = 12$.

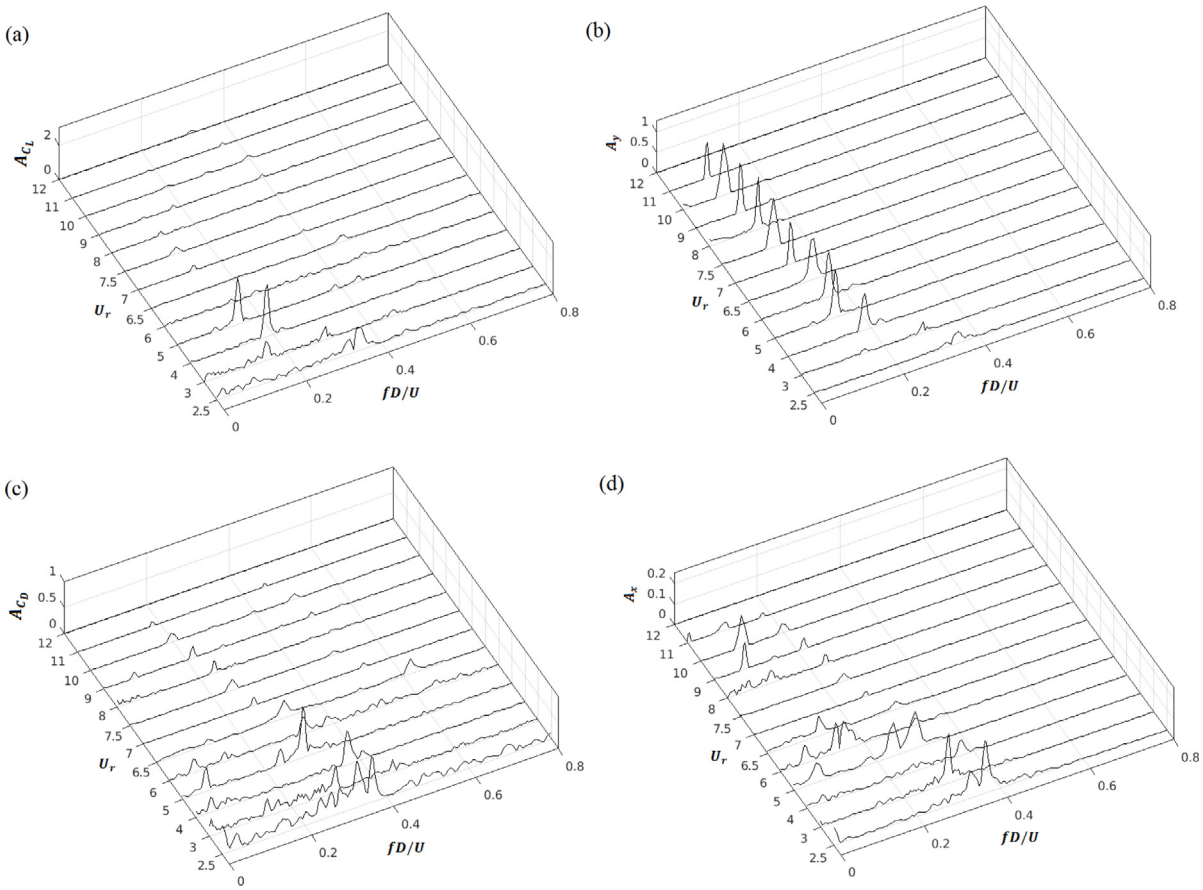

Fig. 12. Frequency spectra of C_L, y/D, C_D and x/D: single cylinder.

discrepancies in the observed $\overline{C}_D$ and St values between the simulations using $Co_{max} = 0.5$ and $Co_{max} = 0.25$ are within 1%. The relative differences in the calculated $A_{y,max}/D$ and $C_{L,rms}$ using $Co_{max} = 0.25$ compared with the values obtained using $Co_{max} = 0.5$ are approximately 1.80% and 3.10%, respectively. Thus, based on the convergence studies with the vibrating single cylinder, it is concluded that the mesh A3 with 104536 elements and $Co_{max} = 0.5$ provides sufficient grid and time step convergence. This setting of mesh and time step is selected for the present simulations of FIV of a single cylinder.

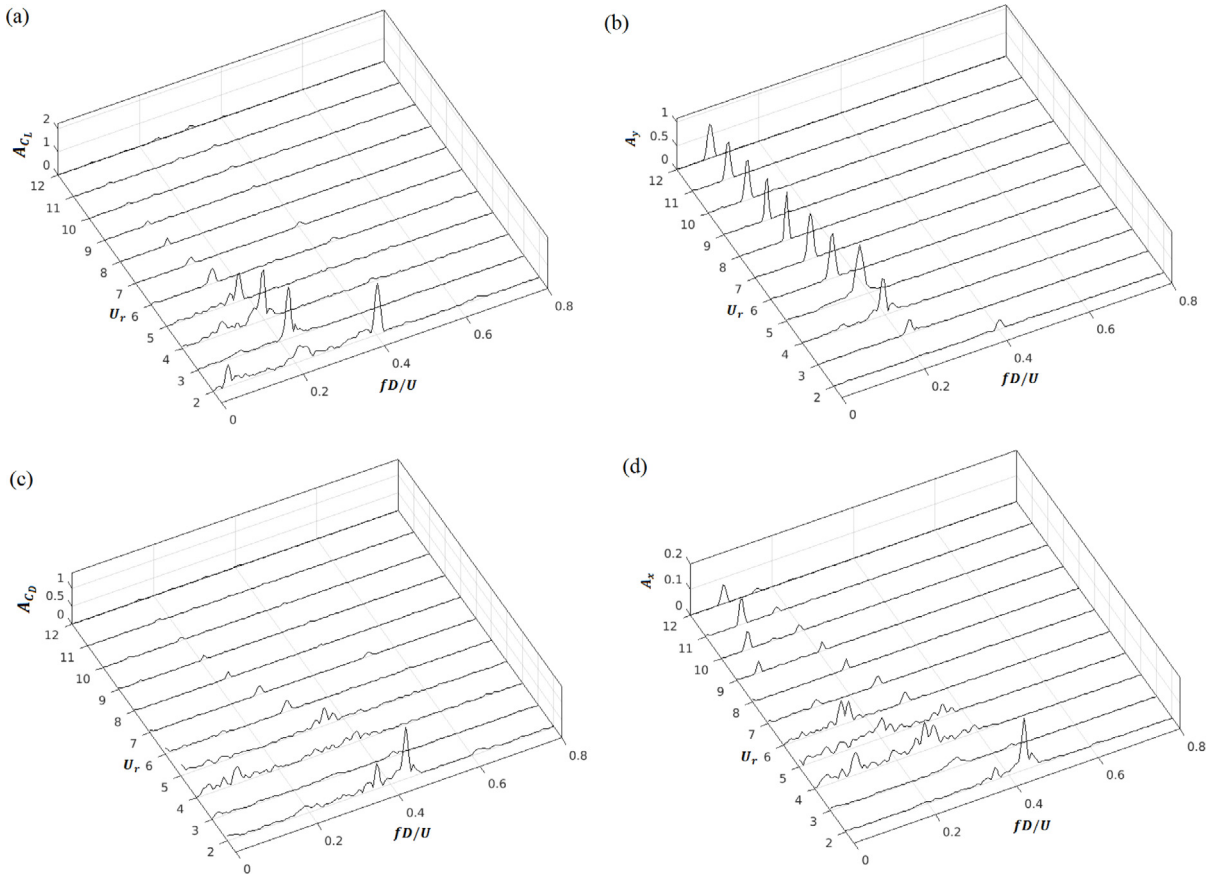

Fig. 13. Frequency spectra of C_L, y/D, C_D and x/D: coupled cylinders $\alpha = 0°$, $G/D = 0.1$.

Table 4
Mesh convergence study for the vibrating single cylinder.

Mesh	No. of cells	Time step	$\overline{C}_D$	$C_{L,rms}$	St	$A_{y,max}/D$
A1	53,595	$Co_{max} = 0.5$	1.2848	0.3659	0.4992	1.1701
A2	74,889	$Co_{max} = 0.5$	1.3120	0.4728	0.4898	1.2907
A3	1,04,536	$Co_{max} = 0.5$	1.2503	0.5134	0.4844	1.2937
A4	1,46,092	$Co_{max} = 0.5$	1.2529	0.5185	0.4844	1.2751

Table 5
Time step convergence study for the vibrating single cylinder.

Mesh	No. of cells	Time step	$\overline{C}_D$	$C_{L,rms}$	St	$A_{y,max}/D$
A3	1,04,536	$Co_{max} = 1.0$	1.3188	0.5194	0.5033	1.3274
A3	1,04,536	$Co_{max} = 0.5$	1.2503	0.5182	0.4844	1.3055
A3	1,04,536	$Co_{max} = 0.25$	1.2612	0.4997	0.4844	1.3170

In the grid resolution analyses for the cases with two coupled cylinders, the computational domain is the same as that for the single cylinder cases. It consists of structured hexahedral elements. Figs. 4 and 5 show a typical mesh for $\alpha = 90°$ and $G/D = 0.1$ configuration used in the convergence studies. Three meshes with an increment of approximately 40% in the total number of elements are assessed.

In Table 6, the results of the grid sensitivity study for the two vibrating coupled cylinders with $\alpha = 90°$ and $G/D = 0.1$ configuration are presented. The maximum Courant number is constrained to 0.5 based on the results obtained from the time step convergence studies with the vibrating single cylinder (Table 5). The reduced velocity $U_r = 6$ is used in the simulations. At this U_r, high amplitudes of the cylinder's vibration are expected, facilitating the assessment of the dynamic simulations convergence. The relative differences in the results between the meshes B2 and B3 are within 1.45% for $\overline{C}_D$, $C_{L,rms}$ and St. The deviation in the calculated $A_{y,max}/D$ using the mesh B3 compared to the obtained result using the mesh

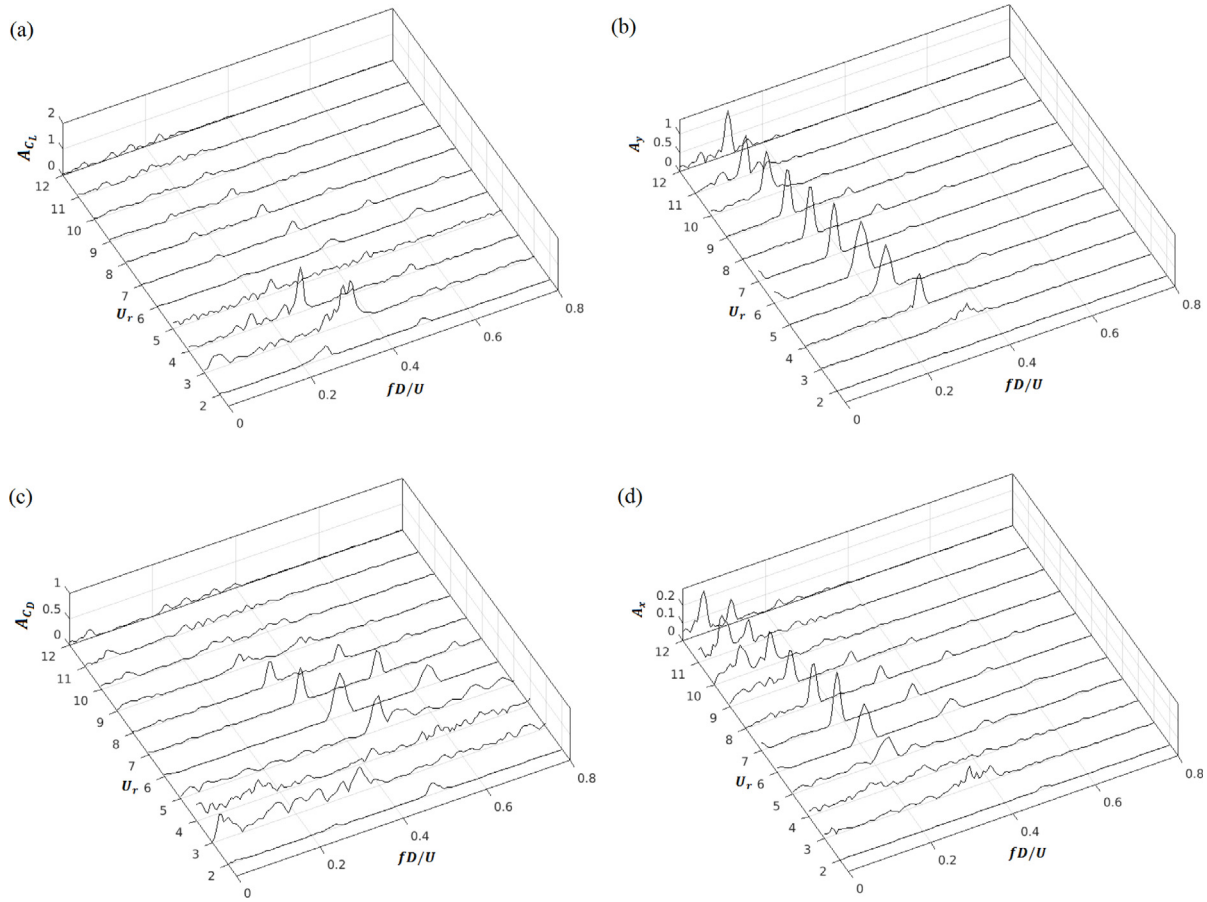

Fig. 14. Frequency spectra of C_L, y/D, C_D and x/D: coupled cylinders $\alpha = 90°$, $G/D = 0.1$.

Table 6
Mesh convergence study for the two vibrating rigidly coupled cylinders with $\alpha = 90°$ and $G/D = 0.1$ configuration.

Large cylinder						
Mesh	No. of cells	Time step	$\overline{C}_D$	$C_{L,rms}$	St	$A_{y,max}/D$
B1	57,833	$Co_{max} = 0.5$	1.6392	0.5218	0.5033	1,4678
B2	80,163	$Co_{max} = 0.5$	1.4844	0.5601	0.5033	1,4355
B3	1,14,321	$Co_{max} = 0.5$	1.4808	0.5534	0.5033	1,4013
Small cylinder						
Mesh	No. of cells	Time step	$\overline{C}_D$	$C_{L,rms}$	St	$A_{y,max}/D$
B1	57,833	$Co_{max} = 0.5$	3.1914	1.9453	0.0841	1,4678
B2	80,163	$Co_{max} = 0.5$	3.6173	2.0196	0.0841	1,4355
B3	1,14,321	$Co_{max} = 0.5$	3.6290	1.9945	0.0841	1,4013

B2 is 2.38%. Considering that further mesh refinement results in negligible change of the compared parameters, the mesh B3 is selected for the present simulations of FIV of two coupled cylinders with different α and G/D.

3.3. Validation studies

The numerical model employed in the present study is validated by comparing the present model predictions for the single stationary cylinder configuration with the published experimental and numerical studies in the upper transition regime. The number of published data in the upper transition regime is very limited since the required experimental setup and numerical simulations to reproduce such flows are very complex and expensive. To the best of the authors' knowledge, there is no available published experimental data for vibrating cylinder in the upper transition regime.

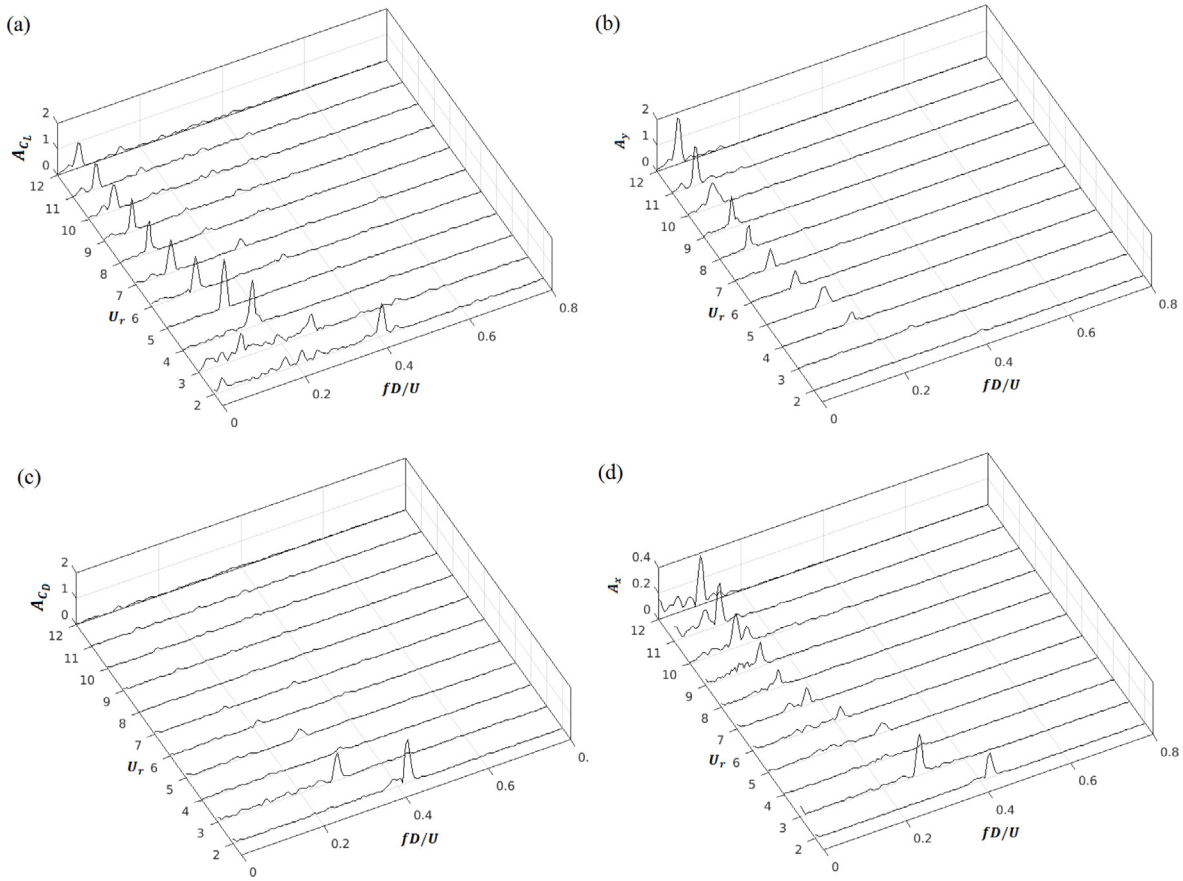

Fig. 15. Frequency spectra of C_L, y/D, C_D and x/D: coupled cylinders $\alpha = 180°$, $G/D = 0.1$.

Table 7
Numerical and experimental data of a single stationary cylinder at high Reynolds number regime.

Author	Description	$\overline{C}_D$	$C_{L,rms}$	$-C_{Pb}$	St
Present study	URANS $k-\omega$SST Re $= 3.6 \times 10^6$	0.4616	0.175	0.5527	0.3204
Catalano et al. (2003)	URANSk $-\epsilon$ Re $= 4 \times 10^6$	0.46	–	–	–
Ong et al. (2009)	URANSk $-\epsilon$ Re $= 3.6 \times 10^6$	0.4573	0.0766	–	0.3052
Porteous et al. (2015)	URANS $k-\omega$SST Re $= 3.6 \times 10^6$	0.4206	–	0.495	0.148
Pang et al. (2016)	URANS $k-\omega$SST Re $= 5.2 \times 10^6$	0.457	0.1847	0.594	0.321
Roshko (1961)	Experimental studies Re $= (1–3.5) \times 10^6$	0.30–0.70	–	0.62–0.85	–
Schmidt (1966)	Experimental study Re $= 5 \times 10^6$	0.533	0.1379	0.605	–
Achenbach (1968)	Experimental studies Re $= (1-5) \times 10^6$	0.37–0.68	–	0.85	–

The predicted values of $\overline{C}_D$, $C_{L,rms}$, $-C_{Pb}$ and St for the single stationary cylinder are compared with available published results in Table 7. The base pressure coefficient (C_{Pb}) is defined here as the value of C_P at $\theta = 180°$ (θ is defined as the peripheral angle of the cylinder measured clockwise from the stagnation point). The predicted $\overline{C}_D$ shows good agreement with the published numerical results reported by Catalano et al. (2003), Ong et al. (2009) and Pang et al. (2016), and the predicted value of $\overline{C}_D$ is also in the range of values reported by Roshko (1961) and Achenbach (1968) using experiments. The present predicted $C_{L,rms}$ is in agreement with the value predicted by Pang et al. (2016). However, it is different from the predicted value of $C_{L,rms}$ reported by Ong et al. (2009) where URANS $k-\varepsilon$ was employed. The predicted $-C_{Pb}$ agrees well with the values reported by Porteous et al. (2015) and Pang et al. (2016). The value of St, on the other hand, is higher than the value predicted by Porteous et al. (2015) but close to the value reported by Ong et al. (2009) and Pang et al. (2016).

Fig. 6 shows the time-averaged pressure distribution and skin friction distribution around the cylinder compared with the experimental data reported by Achenbach (1968) and the numerical results reported by Ong et al. (2009). The time-averaged pressure distribution shows a good agreement with the results reported by Ong et al. (2009). Compared with the data reported by Achenbach (1968), it seems that the present model underpredicts C_P at $60° < \theta < 80°$ and

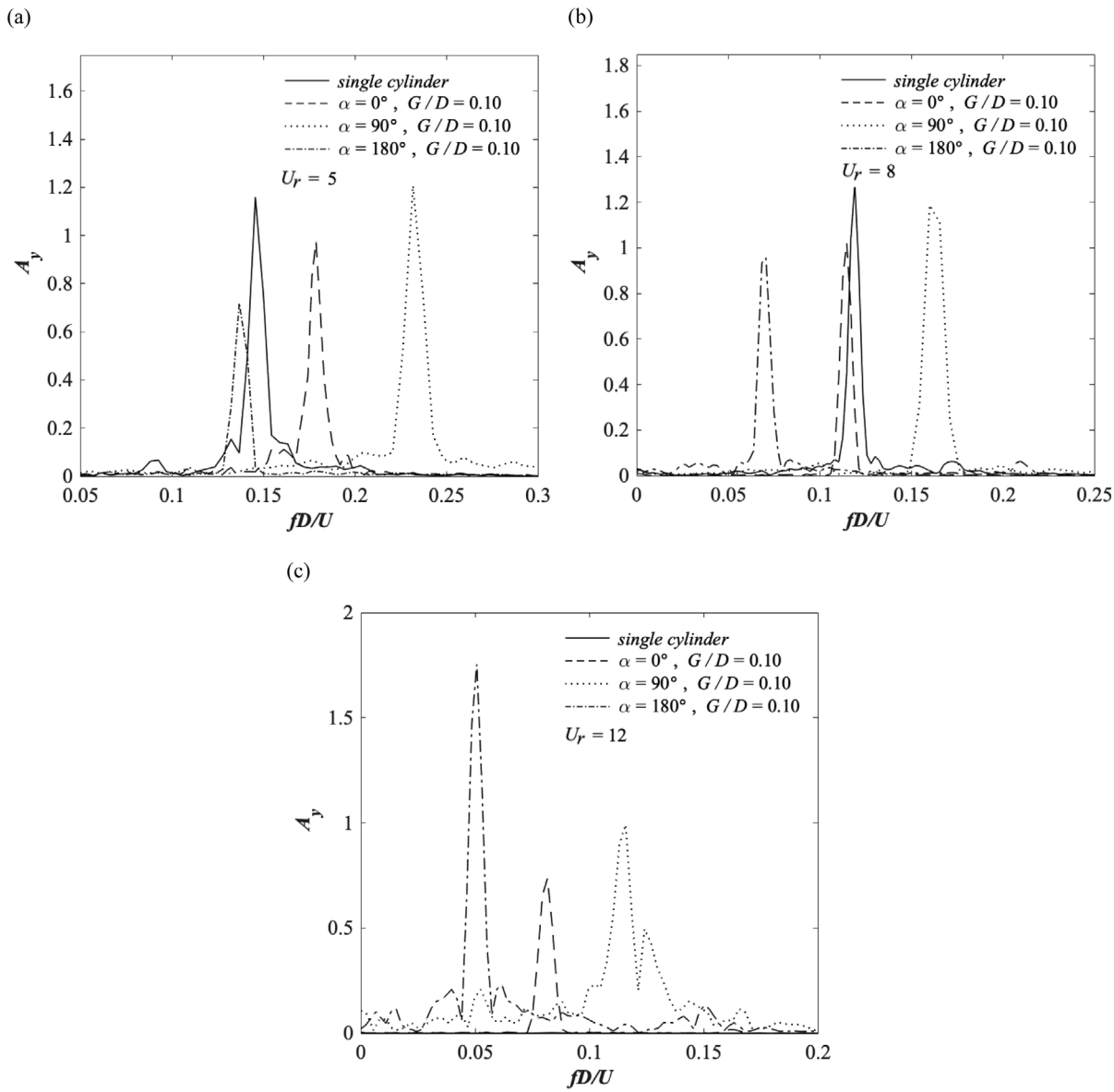

Fig. 16. Frequency spectra of y/D for the single cylinder and $\alpha = [0°, 90°, 180°]$ configurations at selected U_r: (a) $U_r = 5$, (b) $U_r = 8$ and (c) $U_r = 12$.

$110° < \theta < 180°$. In Fig. 6(b), the skin friction distribution has a satisfactory prediction between the present simulation and the published data by Ong et al. (2009) and Achenbach (1968) for the region of separated flow at $113° < \theta < 250°$. The discrepancies observed in the region of attached flow may be attributed to the use of the wall function in predicting the turbulent boundary layer flow around a single cylinder. The present model combined with the wall function assumes that the boundary layer flow near the cylinder wall is fully developed. However, for $\mathrm{Re} < 4 \times 10^6$ the boundary layer around the cylinder is not fully turbulent yet, especially before the separation point where there is a transition from laminar to turbulent boundary layer flow.

Overall, the present numerical model is in good agreement with the published numerical and experimental data.

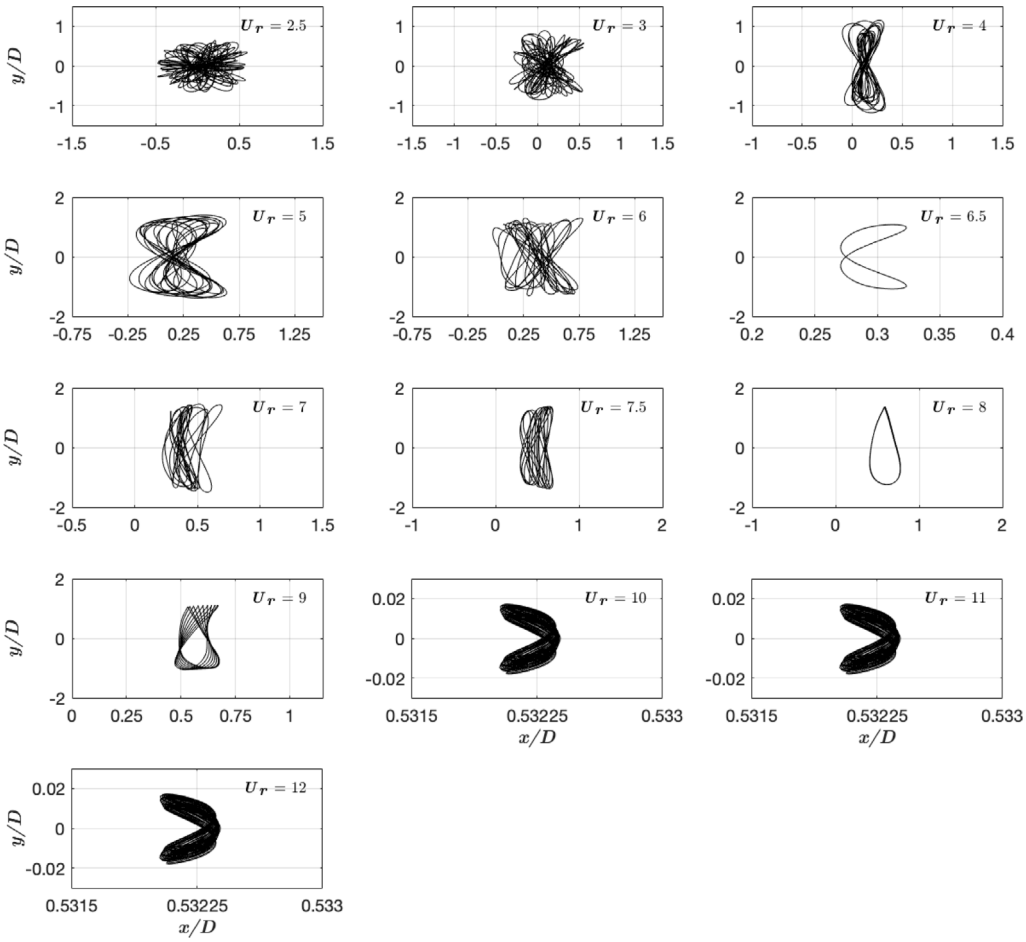

Fig. 17. x/D–y/D trajectory: single cylinder.

4. Results and discussion

4.1. Effect of the position angle α

4.1.1. Hydrodynamic force coefficients

The hydrodynamic force coefficients of the cylinder bundle and the single cylinder configuration are discussed. For the cases with two cylinders, $\overline{C}_D$, $\overline{C}_L$, $C_{D,rms}$ and $C_{L,rms}$ are obtained based on the total force value for both cylinders and their projected area to the flow direction. The corresponding projected areas for drag and lift coefficients in the $\alpha = 0°$ and $\alpha = 180°$ configurations are $1D$ and $1.25D$, respectively. While for the $\alpha = 90°$ configuration, the projected areas are $1.25D$ and $1D$ for the drag and lift coefficients, respectively. Fig. 7 shows the variation of $\overline{C}_D$ and $C_{D,rms}$ with U_r for the single cylinder configuration and all the investigated α configurations with two cylinders. It can be seen that the presence of the small cylinder has a strong influence on $\overline{C}_D$ which has also been reported by Zang and Gao (2014) in the subcritical Reynolds number flow regime. For the single cylinder configuration, the $\overline{C}_D$ values are around 1.2 for $2.5 \leq U_r \leq 6.5$ and tend to decrease for $U_r > 6.5$. Compared with the single cylinder configuration, when the small cylinder is placed upstream the large cylinder ($\alpha = 0°$), an increased magnitude of $\overline{C}_D$ is observed for $4 \leq U_r \leq 5$ with a peak at $U_r = 5$. A decreased magnitude of $\overline{C}_D$ is observed when placing the small cylinder downstream the large cylinder ($\alpha = 180°$) for $U_r < 10$, compared with the single cylinder configuration. For $U_r \geq 11$, the values of $\overline{C}_D$ for the single cylinder and the $\alpha = 0°$ configurations are similar. The highest values of $\overline{C}_D$ are observed when the cylinders are vertically aligned ($\alpha = 90°$) for $4 \leq U_r \leq 6$.

The $C_{D,rms}$ curve presented in Fig. 7(b) shows peak values at low reduced velocities ($U_r \leq 3$) for all the investigated configurations. This is characteristic of in-line lock-in. The highest peak in $C_{D,rms}$ is observed for the single cylinder configuration at $U_r = 2.5$ and it is followed by a sharp decrease with increasing U_r. Similar behavior is observed for the $\alpha = 0°$ and $\alpha = 180°$ configurations, where a peak in $C_{D,rms}$ is observed at $U_r = 2$ for both configurations. The $\alpha = 90°$ configuration has the lowest peak in $C_{D,rms}$ observed at $U_r = 3$, and it is followed by a monotonic decrease.

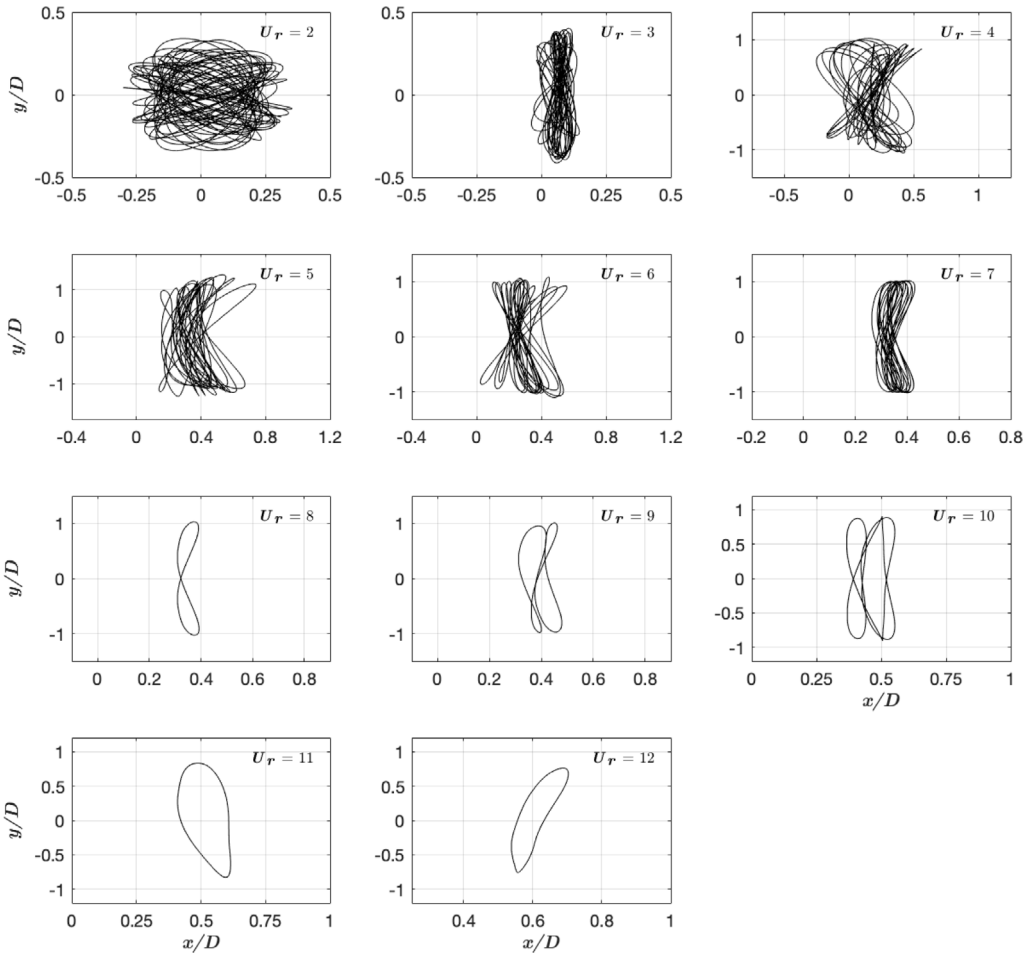

Fig. 18. x/D–y/D trajectory: coupled cylinders $\alpha = 0°$, $G/D = 0.1$.

Fig. 8 shows $\overline{C}_L$ and $C_{L,rms}$ against U_r for the single cylinder configuration and different α configurations. As expected, $\overline{C}_L$ is approximately zero in the configurations characterized by geometric symmetry aligned with the flow direction (single cylinder, $\alpha = 0°$ and $\alpha = 180°$). For the $\alpha = 90°$ configuration, the effect of the small cylinder on $\overline{C}_L$ is significant. Positive values of $\overline{C}_L$ are observed for $4 \leq U_r \leq 10$ with a peak at $U_r = 5$, and negative values of $\overline{C}_L$ are found for $U_r \leq 3$ and $U_r \geq 11$.

Negative $\overline{C}_L$ observed in the stationary $\alpha = 90°$ configuration has been reported in numerous experimental (Tsutsui et al., 1997; Kalghatgi and Sayer, 1997) and numerical studies (Tsutsui et al., 1997; Zhao et al., 2007; Thapa et al., 2015). When the cylinder bundle is free to vibrate with 2-DoF, the switch in the direction of the mean lift force may occur in the lock-in range. Zang and Gao (2014) reported positive mean lift for vibrating piggyback cylinders at Re $= 3.4 \times 10^4$ in the lock-in region. Similar observations were made by Rahmanian et al. (2012) employing 2D URANS simulations at Re $= 8 \times 10^4$ and $U_r = 8$. Shedding of the clockwise vortices induces lift force in negative direction (Jauvtis and Williamson, 2004). In the lock-in range (Fig. 23, $U_r = 3$ – 11), the interaction between the vortex shedding from the small cylinder and the development of the clockwise vortices on the upper side of the large cylinder results in changes in the mean pressure distribution around the cylinders bundle. Fig. 9 shows the time-averaged C_p distribution for the small and large cylinders ($\alpha = 90°$, $G/D = 0.1$ configuration) for different U_r. It can be seen that in the lock-in range ($U_r = 5$ and $U_r = 8$ in Fig. 9), the C_p distribution is highly asymmetric with larger negative areas on the upper side of the large cylinder as shown in Fig. 9 in the range of $\theta = 60°$–$120°$. There is a characteristic bump in the C_p on the lower side of the large cylinder as shown in Fig. 9 in the range of $\theta = 260°$–$300°$.

The peak values of the $C_{L,rms}$ curve for the single cylinder, $\alpha = 0°$ and $\alpha = 90°$ configurations are found at $U_r \leq 5$, and a sudden decrease occurs with increasing U_r. The $C_{L,rms}$ curve for the $\alpha = 180°$ configuration shows less variability in the range of the studied U_r, compared with the other configurations. Also, for $6 \leq U_r \leq 12$, the observed $C_{L,rms}$ values for the $\alpha = 180°$ cases are higher than those for the other configurations.

In general, the highest values of $\overline{C}_D$ and $C_{L,rms}$ are observed for $\alpha = 90°$ configuration. This behavior is also observed in the subcritical Reynolds number regime according to Rahmanian et al. (2012).

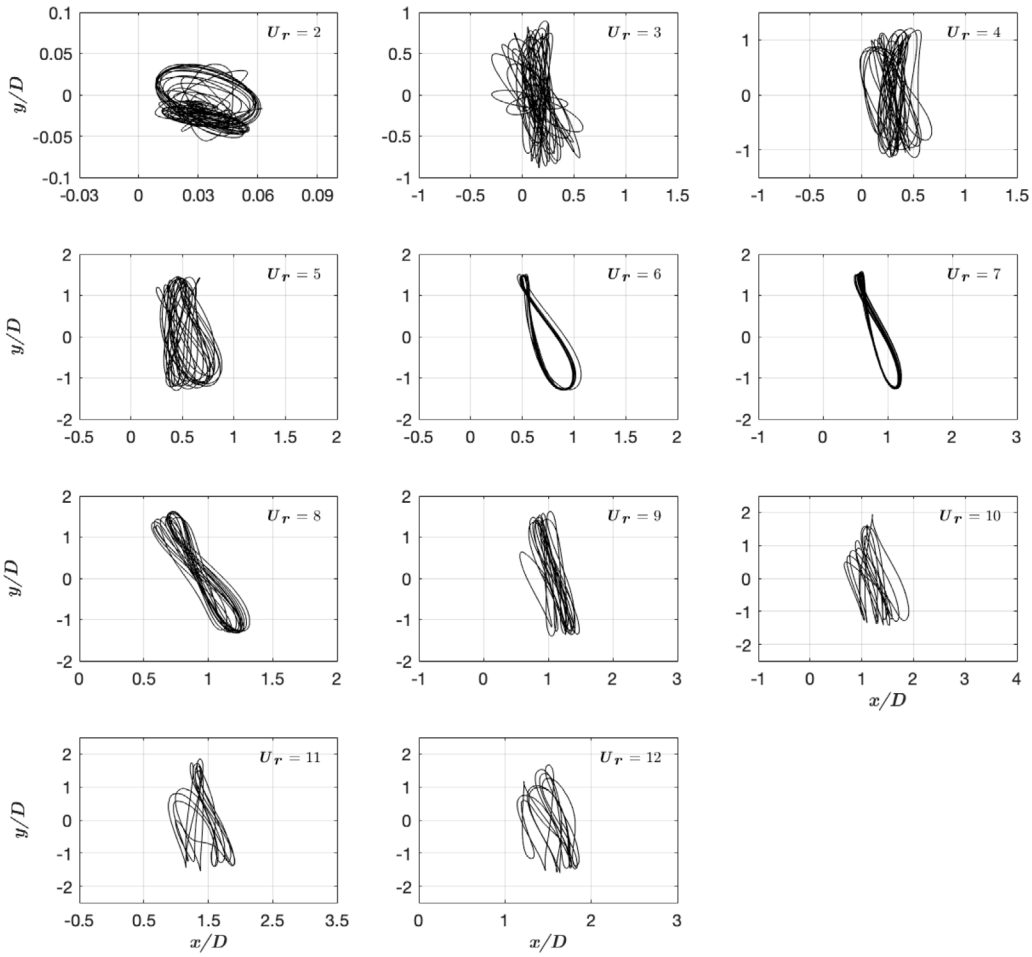

Fig. 19. x/D–y/D trajectory: coupled cylinders $\alpha = 90°$, $G/D = 0.1$.

4.1.2. Vibration amplitude response

The variation of $A_{y,max}/D$ and the root-mean-square of the in-line vibration amplitude $A_{x,rms}/D$ with U_r is presented in Fig. 10. The expression for the normalized root-mean-square of the in-line vibration amplitude is given by:

$$\frac{A_{x,rms}}{D} = \frac{\sqrt{\left[\sum_{i=1}^{n}\left(A_{x,i} - \overline{A}_x\right)^2\right]/n}}{D} \tag{22}$$

Based on the $A_{y,max}/D$ curve, the lock-in regime of the single cylinder configuration is observed in the range of $2.5 \leq U_r \leq 11$ where $A_{y,max}/D > 0.5$. The peak value of approximately $A_{y,max}/D = 1.52$ occurs at $U_r = 8$ which is in accordance with Jauvtis and Williamson (2004). At $U_r = 12$, $A_{y,max}/D$ is approximately zero, thus the lock-in has terminated. Compared with the $A_{y,max}/D$ value found by Zang and Gao (2014) in the subcritical Reynolds number flow regime, $A_{y,max}/D$ is twice and the corresponding U_r is very similar. A narrower lock-in range is observed for the low Reynolds number flow regime in Zhao and Yan (2013) with $A_{y,max}/D = 0.62$. The lock-in regime of the three investigated α configurations extends beyond the studied range of U_r, where $A_{y,max}/D > 0.5$ is observed at $U_r = 12$. For the $\alpha = 0°$ configuration, the peak of $A_{y,max}/D = 1.26$ occurs at $U_r = 5$ and the lock-in starts at $U_r = 2$.

For the $\alpha = 90°$ and $\alpha = 180°$ configurations, $A_{y,max}/D$ values increase monotonically over the range of investigated U_r. Galloping is a flow-induced vibration phenomenon arising when the rotational symmetry of the cross-section is not present (Paidoussis, 2010). According to Zhao et al. (2014, 2018), both VIV and galloping may occur at the same time. They reported that in the transition regime from VIV to galloping the fluid forcing frequency response undergoes changes with respect to dominant frequencies in the spectrum. The third harmonic of the lift force (f_{CL}) gradually becomes stronger than its first harmonic in this regime, indicating that the vortex shedding frequency becomes higher than that of the body oscillation. To investigate the extended range of the high cross-flow amplitude response observed for the $\alpha = 90°$ and $\alpha = 180°$ configurations, Fast Fourier Transform (FFT) plots of the lift force and the cross-flow displacement time series

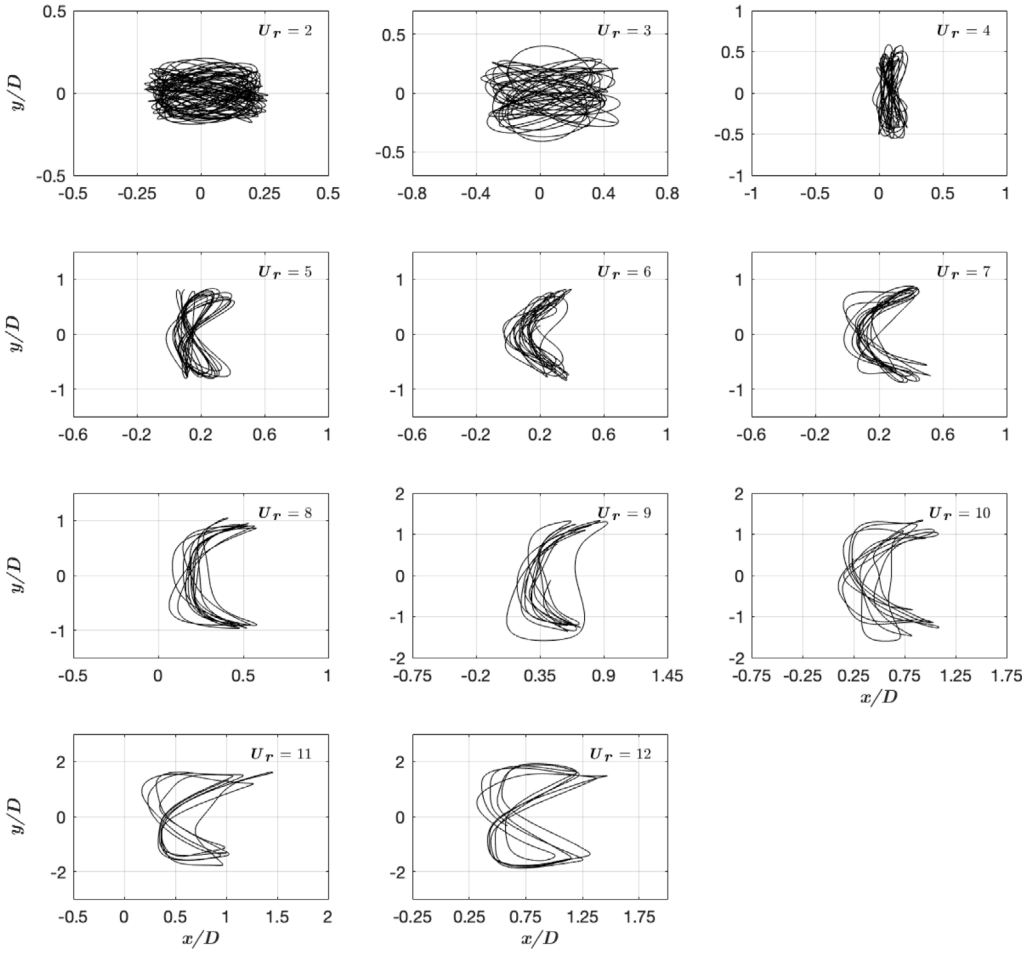

Fig. 20. x/D–y/D trajectory: coupled cylinders $\alpha = 180°$, $G/D = 0.1$.

are provided (Fig. 11). The frequencies are normalized by the dominant frequency of the cross-flow vibration, i.e. f/f_{osc}. In both cases shown in Fig. 11 there is a peak in the frequency spectra of C_L at the third harmonic ($f/f_{osc} = 3$). However, it is not the dominant frequency in the C_L spectra. In the C_L frequency spectrum of the $\alpha = 90°$ configuration the dominant frequency of C_L is observed at the second super harmonic ($f/f_{osc} = 2$) and a strong influence of $f/f_{osc} = 1$ and $f/f_{osc} = 0.5$ components is present. In the C_L frequency spectrum of the $\alpha = 180°$ configuration the dominant frequency of C_L is located at $f/f_{osc} = 1$. These findings suggest that the cross-flow vibration responses of the $\alpha = 90°$ and $\alpha = 180°$ configurations are VIV dominated at the upper range of the investigated U_r. However, a noticeable third harmonic content in the C_L spectra may indicate the onset of transition to galloping regime as described by Zhao et al. (2018).

The highest $A_{y,max}/D$ is observed for the $\alpha = 180°$ configuration with $A_{y,max}/D = 2.61$ at $U_r = 12$. In general, the observed values of $A_{y,max}/D$ for the coupled cylinder cases are significantly higher than the same for the subcritical Reynolds number flow regime (Rahmanian et al., 2012).

The $A_{x,rms}/D$ curves for the single cylinder and the $\alpha = 0°$ configurations (Fig. 10(b)) are characterized by a non-monotonic behavior. However, there is a visible trend of decrease in the $A_{x,rms}/D$ values with increasing U_r. On the other hand, for the $\alpha = 90°$ and $\alpha = 180°$ configurations, the values of $A_{x,rms}/D$ show a trend to increase with increasing U_r.

4.1.3. Frequency analysis

Fast Fourier Transform is used to compute the frequency spectra of C_L, C_D, y/D and x/D. The frequency spectra are shown in Figs. 12–15 for the single cylinder, $\alpha = 0°$, $\alpha = 90°$ and $\alpha = 180°$ configurations, respectively. The frequency spectra are presented in the $U_r - fD/U$ plane. For the single cylinder, $\alpha = 0°$ and $\alpha = 90°$ configurations, the initial branch is characterized by distinct C_L peak frequencies. For the $\alpha = 180°$ configuration, the C_L peak frequencies are observed for the entire U_r range due to the extended initial branch compared with the other configurations. This behavior is in accordance with Fig. 10(a). Moreover, the dominant frequencies of y/D correspond to the lock-in regimes observed for all

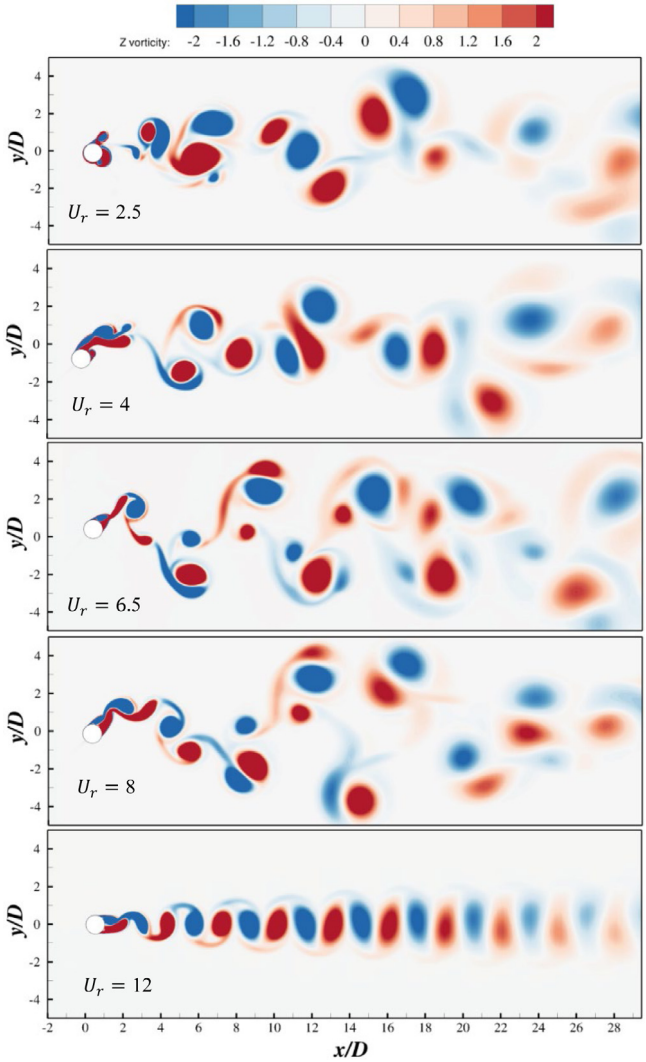

Fig. 21. Vortex shedding patterns at selected U_r: single cylinder.

the configurations. It is observed that the highest amplitudes in the y/D spectra are located in the low frequency range of $fD/U < 0.4$. For all the configurations, the peak frequencies of the spectra decrease with increasing U_r.

The frequency spectra of y/D for the single cylinder, $\alpha = 0°$, $\alpha = 90°$ and $\alpha = 180°$ configurations are shown in Fig. 16 for selected U_r cases. They correspond to the cases with the largest transverse amplitude of displacement found in the respective configurations (see Fig. 10(a)). It can be observed that when $\alpha = 180°$, the dominant frequency is the lowest compared with the other configurations. The $\alpha = 90°$ configuration has the highest peak frequencies at the selected U_r cases. When $U_r = 12$, the single cylinder has the lowest amplitude of response. This is explained by the desynchronization from the vortex shedding at this U_r. Moreover, the $\alpha = 90°$ and $\alpha = 180°$ configurations experience extended lock-in range, up to $U_r = 12$ which is the limit of the present study (see Fig. 10(a)).

4.1.4. Motion trajectories

Figs. 17–20 show the motion trajectories on the x/D–y/D plane for the single cylinder and $\alpha = [0°, 90°, 180°]$ configurations, respectively. The duration of the displacement time series used to plot the motion trajectories is $\tau = 100$. For low U_r values, the trajectory of the single cylinder is characterized by an irregular motion due to large in-line displacement, as shown in Fig. 17. According to Jauvtis and Williamson (2004), in the VIV of a low-mass ratio system with 2-DoF, the characteristic "figure of eight" trajectory is often observed in the initial branch. This trajectory is seen for $U_r = 4$, $U_r = 5$and $U_r = 6$. For $U_r \geq 10$, the trajectory is characterized by small in-line motion. At $U_r = 12$, the structural response is desynchronized from the vortex shedding (see Fig. 10(a)), thus the in-line and cross-flow amplitudes are almost zero.

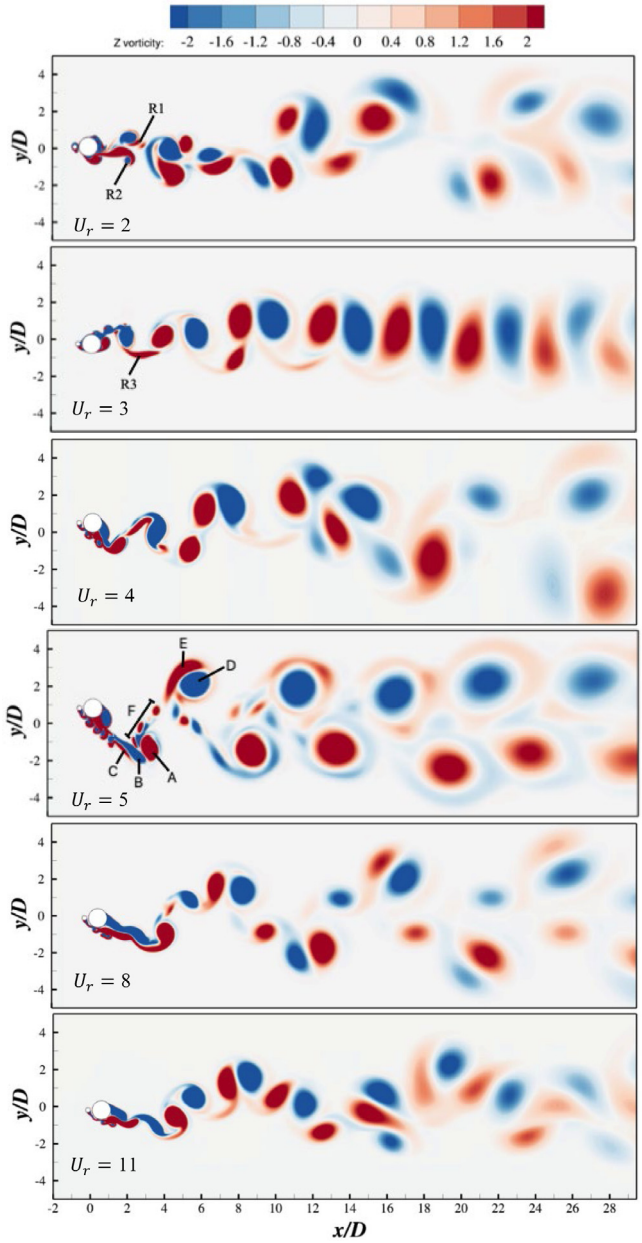

Fig. 22. Vortex shedding patterns at selected U_r: coupled cylinders $\alpha = 0°$, $G/D = 0.1$.

For the $\alpha = 0°$ configuration at $U_r = 2$ (Fig. 18), an irregular trajectory is observed. For $U_r \geq 7$, the trajectories are regular and characterized by small in-line motion. The "figure of eight" is observed at $U_r = 7$, $U_r = 8$and $U_r = 9$. The trajectories in $U_r = 11$ and $U_r = 12$ cases have a skewed oval shape.

The $\alpha = 90°$ cases with $G/D = 0.1$, shown in Fig. 19, have irregular trajectories compared with the single cylinder and $\alpha = 0°$ configurations. The presence of the small cylinder on top of the large cylinder causes the structure at $U_r = 2$ to experience almost zero displacement amplitude, both in the in-line and cross-flow directions. The $U_r = 6, 7$and8 cases are characterized by the "figure of eight" trajectory. For $U_r \geq 7$, the trajectories become more random.

The trajectories of the $\alpha = 180°$ configuration at $U_r = 2$ and $U_r = 3$ are irregular, as shown in Fig. 20. For $5 \leq U_r \leq 9$, the trajectories resemble the crescent shape as reported in Jauvtis and Williamson (2004). The "figure of eight" trajectory is observed for $U_r \geq 10$. Overall, with the increasing U_r, the cross-flow amplitude increases as observed in Fig. 10(a).

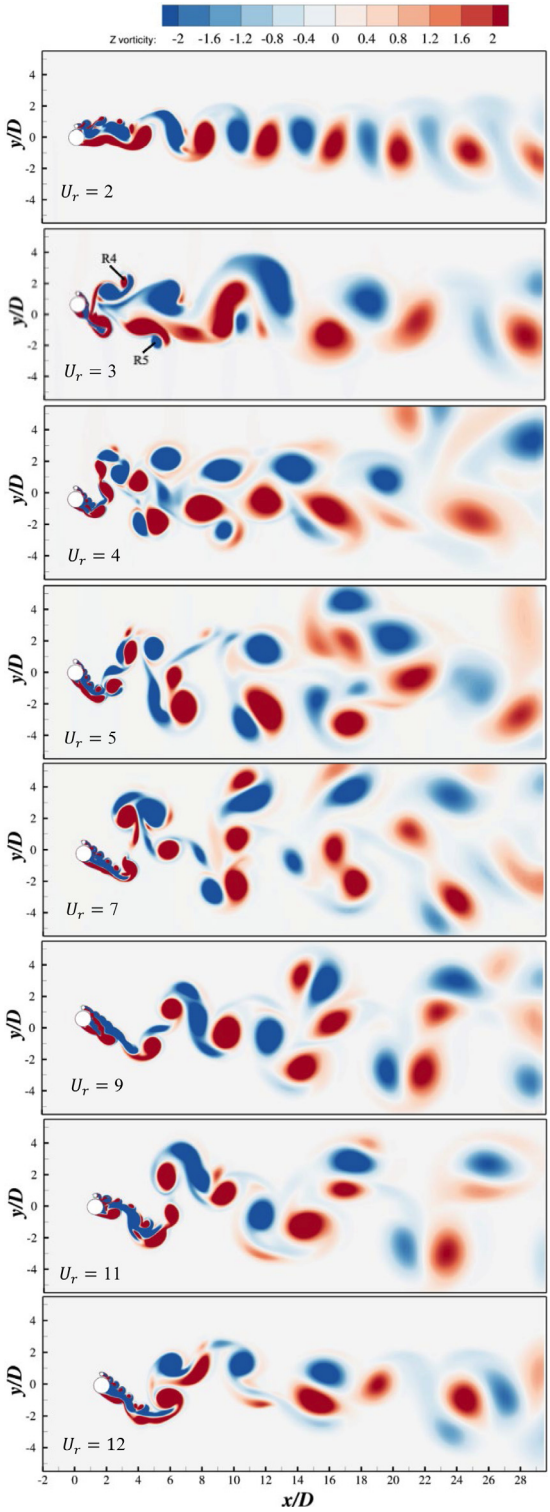

Fig. 23. Vortex shedding patterns at selected U_r: coupled cylinders $\alpha = 90°$, $G/D = 0.1$.

4.1.5. Flow field analysis

The flow characteristics around the single cylinder and the different α configurations are analyzed. Contours of the spanwise vorticity are investigated at selected U_r. The presented flow fields correspond to the cases with different wake

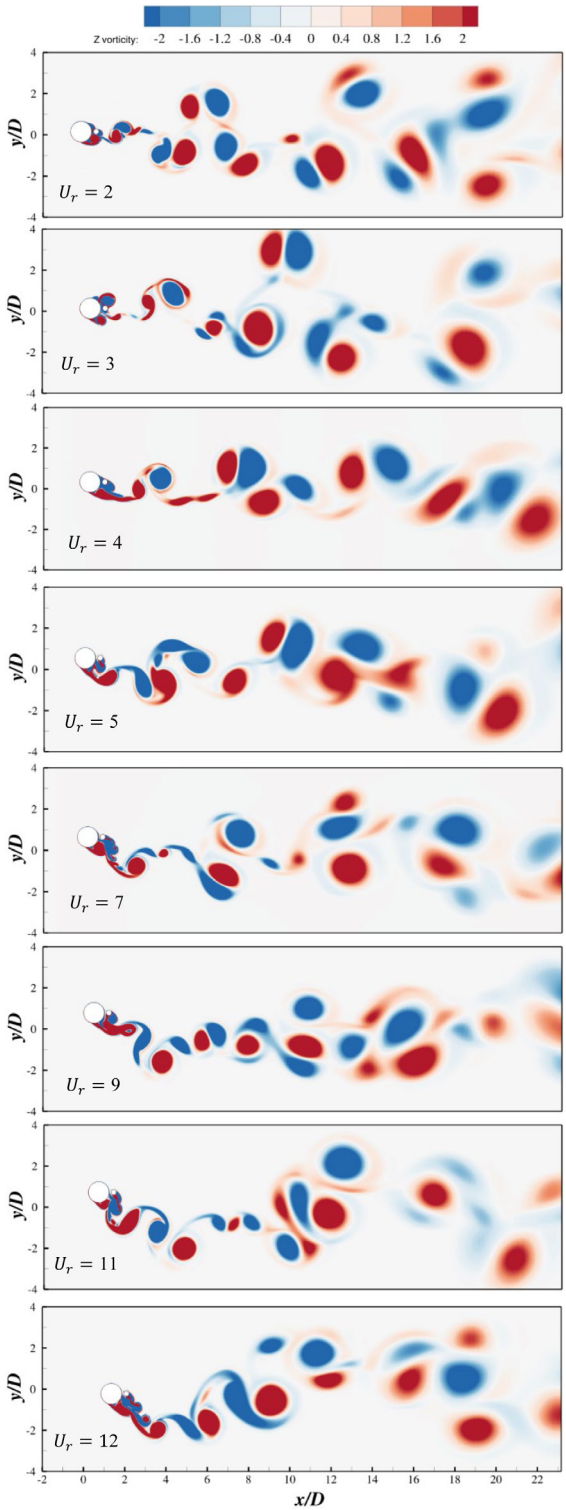

Fig. 24. Vortex shedding patterns at selected U_r: coupled cylinders $\alpha = 180°$, $G/D = 0.1$.

patterns. Firstly, the flow features of the single cylinder configuration are shown in Fig. 21. When $U_r \leq 3$, the vortex shedding pattern is similar to 2S. The far-wake appears to be irregular and unsteady which can be explained by the in-line lock-in experienced by the cylinder at this range of U_r. As U_r is increased ($U_r \geq 4$) the vortex formation length is

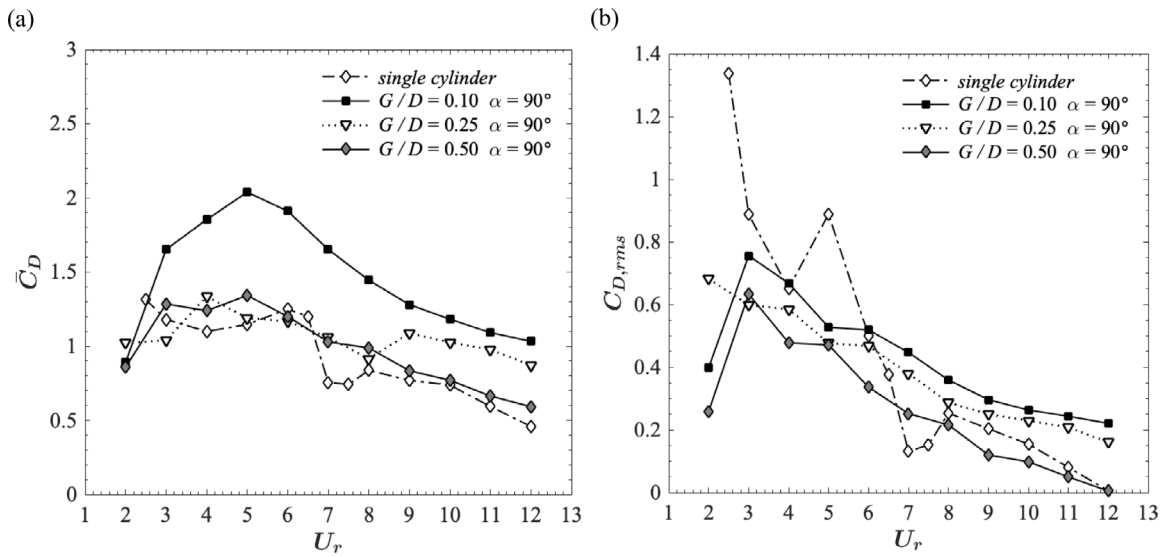

Fig. 25. Time-averaged drag coefficient $\overline{C}_D$ (a) and the root-mean-square of the drag coefficient $C_{D,rms}$ (b) for the single cylinder and $G/D = [0.1, 0.25, 0.5]$ configurations.

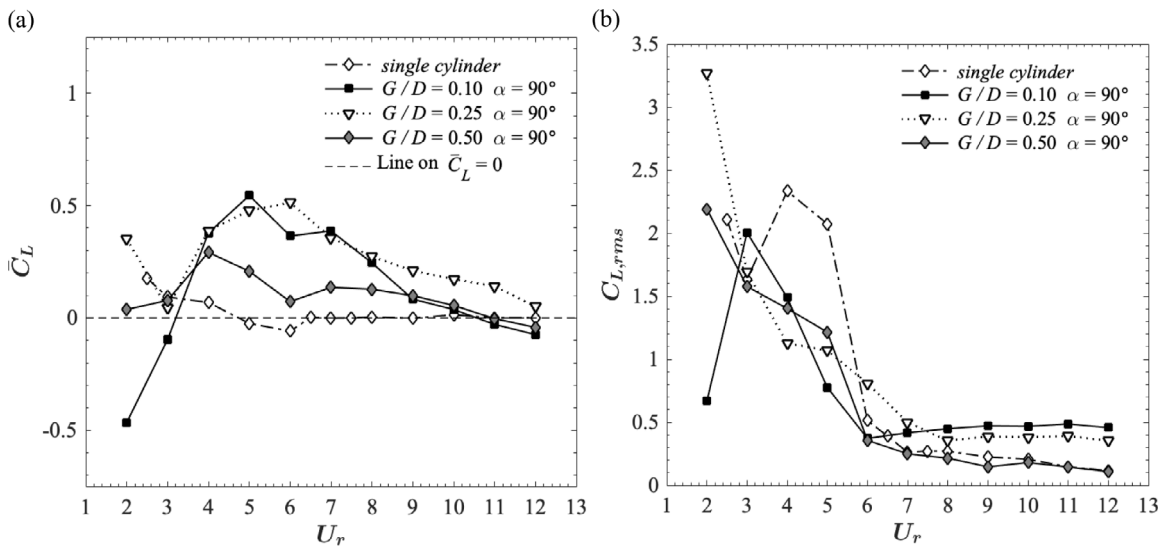

Fig. 26. Time-averaged lift coefficient $\overline{C}_L$ (a) and root-mean-square of the lift coefficient $C_{L,rms}$ (b) for the single cylinder and $G/D = [0.1, 0.25, 0.5]$ configurations.

increased and the vortices stay attached to the cylinder surface for a longer period of time compared with $U_r \leq 3$. The 2T mode can be clearly seen for $6.5 \leq U_r \leq 10$ which is characteristic of the upper branch of lock-in. At $U_r = 12$, the single cylinder response is desynchronized from the vortex shedding, and the wake pattern can be classified as 2S.

Fig. 22 shows the flow characteristics around the $\alpha = 0°$ configuration. At $U_r \leq 3$, the vortex shedding pattern is similar to 2S. It is observed that the presence of the small cylinder generates additional vortices (R1, R2 and R3) in the wake of the cylinders. For $U_r \geq 5$, the presence of the small cylinder increases the vortex formation length from the large cylinder. Moreover, at $U_r = 5$, the vortex street from the small cylinder suppresses the development of a third vortex (C). It is observed that two pairs of vortices (A+B and D+E) are shed with residual vorticity (F) from the suppressed vortex (C) and the vortices shed from the small cylinder. In this case, the vortex shedding pattern can be classified as 2P. When $U_r \geq 8$, the third vortex is not suppressed by the small cylinder and two vortex triplets are shed.

The flow features of the $\alpha = 90°$ configuration are presented in Fig. 23. When $U_r = 2$, the wake pattern seems regular and can be classified as 2S. At this U_r, it is observed that the vortices shed from the small cylinder merge with the vortices behind the large cylinder. The 2S pattern is also seen at $U_r = 3$, but in this case, large vortical structures are formed in

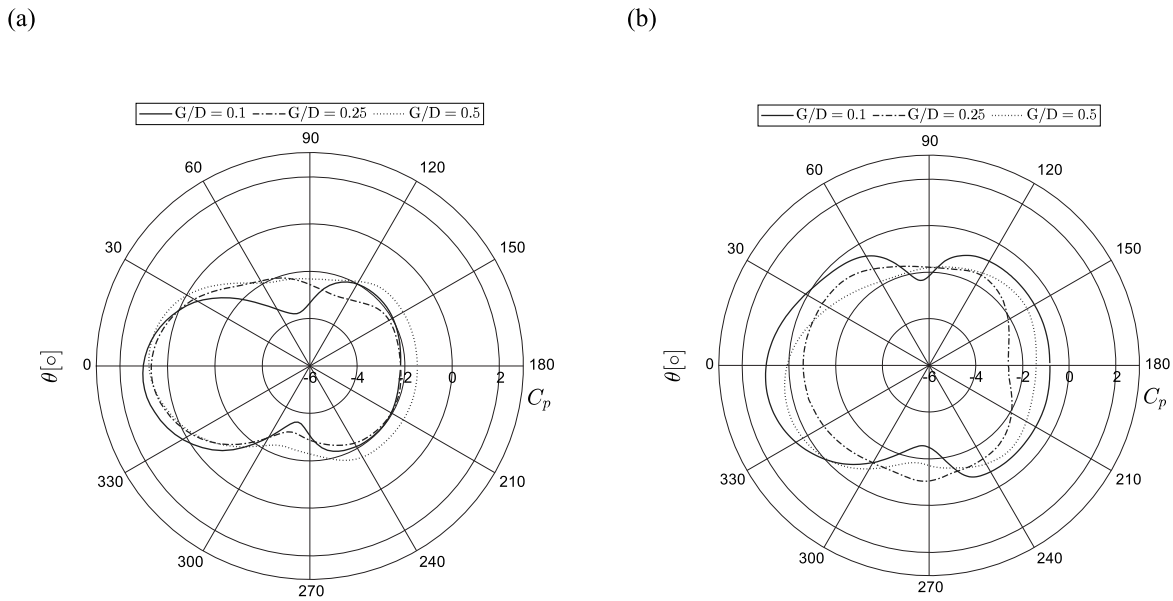

Fig. 27. Pressure coefficient distributions for the (a) small and (b) large cylinders at $U_r = 2$ and different G/D.

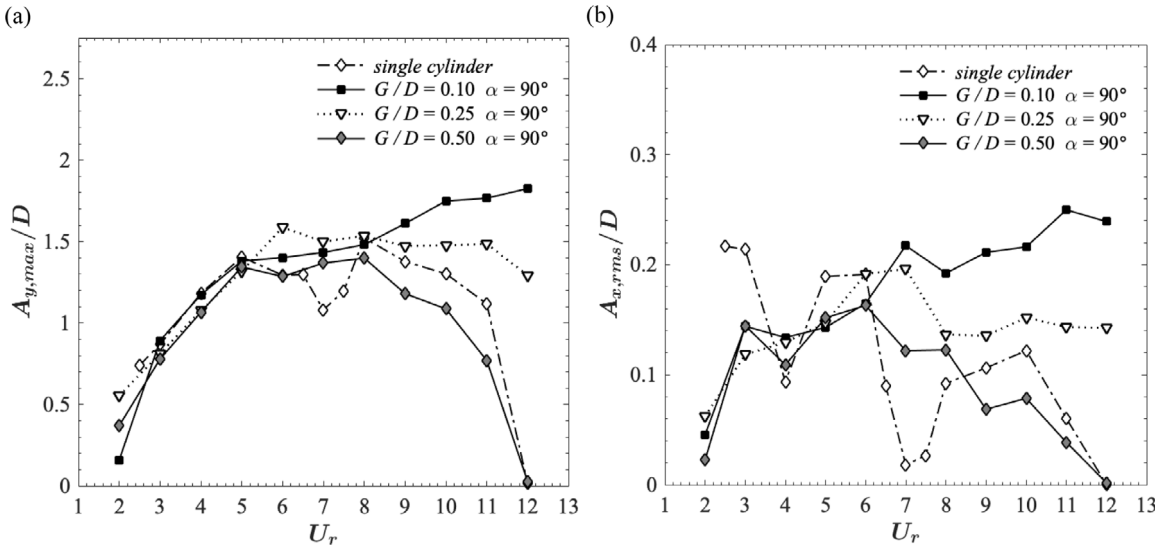

Fig. 28. Normalized maximum cross-flow vibration amplitude $A_{y,max}/D$ (a) and normalized root-mean-square of the in-line vibration amplitude $A_{x,rms}/D$ (b) for the single cylinder and $G/D = [0.1, 0.25, 0.5]$ configurations.

the wake of the cylinders with residual vortices (R4 and R5). With increasing U_r, the presence of the small cylinder affects more the vortex shedding from the large cylinder compared with $U_r = 2$ and 3, and many vortical structures are observed in the wake of the cylinders. At $U_r = 7$, the cylinder bundle sheds a pair of vortices on the upper side, and a triplet on the lower side. When $9 \leq U_r \leq 11$, a pair of vortices is shed on the lower side of the cylinder bundle and a triplet on the upper side. A long vortex street length is seen behind the small cylinder for $U_r \geq 7$. A regular vortex shedding pattern, typical of VIV, is not observed.

Fig. 24 shows the flow fields of the $\alpha = 180°$ configuration. At $U_r = 2$, the vortex shedding pattern is similar to 2P mode. The vortex street behind the small cylinder is visible at $U_r = 7,\ 11$and 12. Similar to the observations made for the $\alpha = 90°$ configuration, a regular vortex shedding pattern is not identified for the $\alpha = 180°$ configuration.

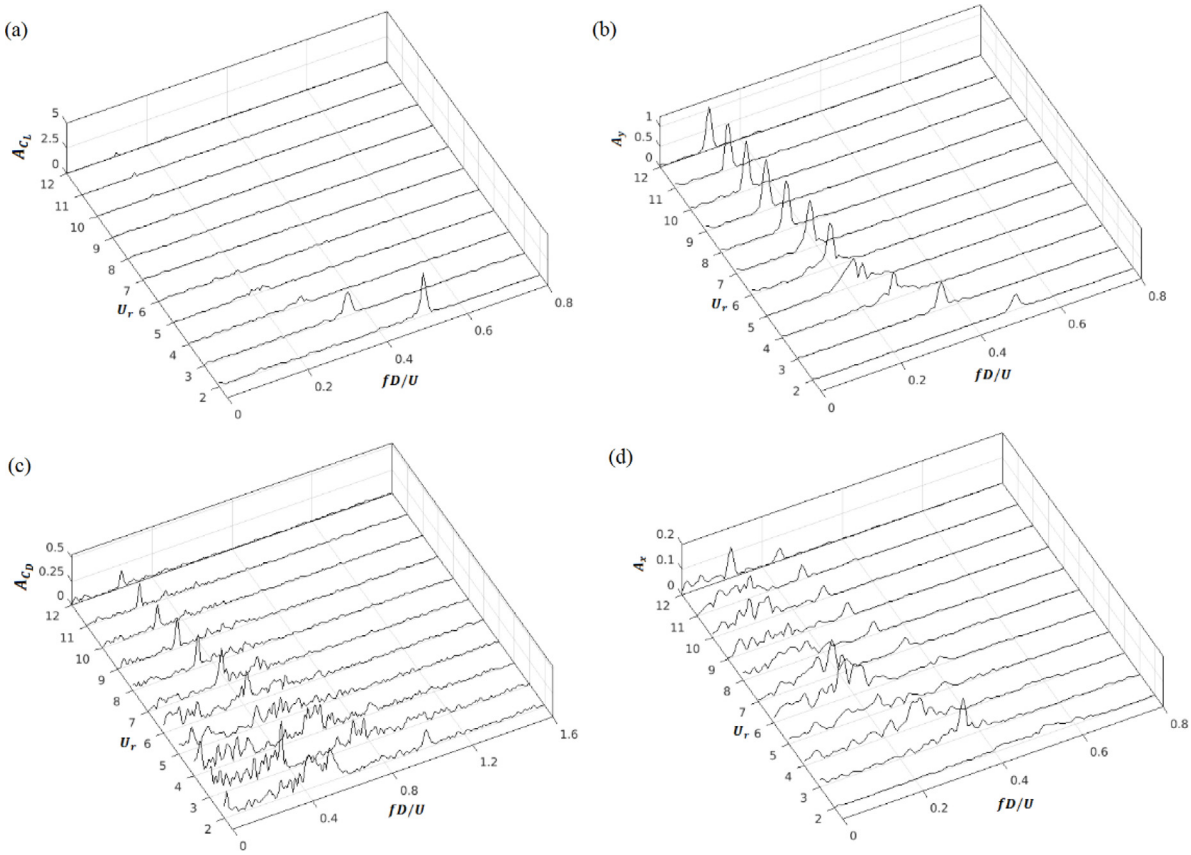

Fig. 29. Frequency spectra of C_L, y/D, C_D and x/D: coupled cylinders $\alpha = 90°$, $G/D = 0.25$.

4.2. Effect of the gap between the cylinders G/D

4.2.1. Hydrodynamic force coefficients

Fig. 25 illustrates the values of $\overline{C}_D$ and $C_{D,rms}$ versus U_r for the single cylinder and the studied G/D configurations. It can be observed that with the increase of G/D, $\overline{C}_D$ values are converging to the values observed for the single cylinder configuration. For $3 \leq U_r \leq 9$, the $G/D = 0.1$ configuration has the highest values of $\overline{C}_D$, with a peak at $U_r = 5$. Among the two coupled cylinder configurations, the $G/D = 0.5$ configuration has the lowest values of $\overline{C}_D$, and the $\overline{C}_D$ curve is the closest to that of the single cylinder configuration. The $\overline{C}_D$ curve for the $G/D = 0.25$ configuration lies in between those of the $G/D = 0.1$ and $G/D = 0.5$ configurations. The $C_{D,rms}$ values observed for the single cylinder configuration (Fig. 25(b)) show considerably more fluctuations compared with those for the other investigated configurations. The $C_{D,rms}$ curves of the two coupled cylinder cases are characterized by peak values at low U_r, $U_r \leq 3$, and a monotonic decrease with increasing U_r. The peak in $C_{D,rms}$ for the $G/D = 0.1$ and $G/D = 0.5$ configurations occurs at $U_r = 3$, and for the $G/D = 0.25$ case, it is observed at $U_r = 2$. In general, $\overline{C}_D$ values reduce with increasing G/D, which was also observed in the subcritical Reynolds number regime in Rahmanian et al. (2012).

Fig. 26 presents the $\overline{C}_L$ and $C_{L,rms}$ curves of the single cylinder and the investigated G/D configurations. It is shown in Fig. 26(a) that the presence of the small cylinder at different G/D values causes non-zero values of $\overline{C}_L$. The highest values of $\overline{C}_L$ are observed for the $G/D = 0.1$ and $G/D = 0.25$ configurations. For the $G/D = 0.5$ configuration, the $\overline{C}_L$ curve is closer to that of the single cylinder compared with the $G/D = 0.1$ and $G/D = 0.25$ configurations. This was also observed by Zang and Gao (2014) for the subcritical Reynolds number flow regime, in which the magnitude of $\overline{C}_L$ increases with increasing G/D until approximately $G/D = 0.25$. For $G/D > 0.25$, $\overline{C}_L$ decreases and converges to the values observed for the single cylinder configuration.

The shape of the $C_{L,rms}$ curve (Fig. 26(b)) for the $G/D = 0.5$ and $G/D = 0.25$ configurations is characterized by a peak value at $U_r = 2$ followed by a sharp decrease. The peak in $C_{L,rms}$ observed for the $G/D = 0.25$ configuration is significantly higher than the predicted values of $C_{L,rms}$ for the other configurations. For $U_r > 6$, the $C_{L,rms}$ values for the single cylinder and the $G/D = 0.5$ configurations converge to similar values and decrease with increase G/D. This behavior is similar to the subcritical Reynolds number flow regime found in Rahmanian et al. (2012). Finally, the $C_{L,rms}$ values for the $G/D = 0.1$ configuration at $U_r > 7$ are the highest among the investigated configurations.

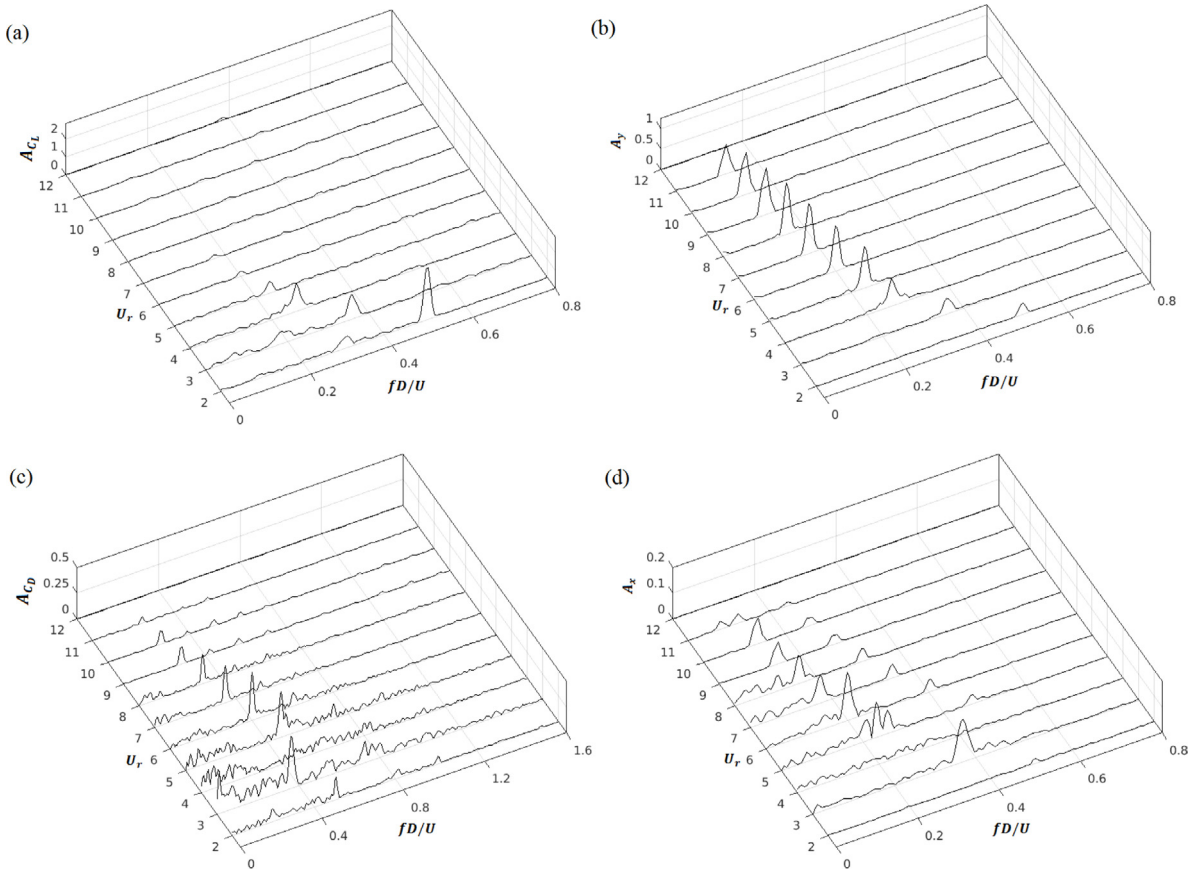

Fig. 30. Frequency spectra of C_L, y/D, C_D and x/D: coupled cylinders $\alpha = 90°$, $G/D = 0.5$.

Fig. 27 presents the time-averaged C_p distribution for the small and large cylinders in the $\alpha = 90°$ configuration at $U_r = 2$ for different G/D. The direction of the mean lift force at $U_r = 2$ is highly sensitive with respect to G/D. With an increase in G/D from 0.1 to 0.25 the C_p distribution around the small cylinder becomes much more asymmetric, with a weaker suction on the upper side of the small cylinder as shown in Fig. 27(a) in the range of θ = 30°–90°. The C_p distribution around the large cylinder (Fig. 27(b)) is characterized by a stronger suction on the upper surface and weaker suction on the bottom surface which results in a positive mean lift force.

4.2.2. Vibration amplitude response

The $A_{y,max}/D$ and $A_{x,rms}/D$ curves for the single cylinder and the different G/D configurations are presented in Fig. 28. It is observed (see Fig. 28(a)) that the lock-in regime for the single cylinder and the $G/D = 0.5$ configurations are captured within the range of the studied U_r. Non-zero $A_{y,max}/D$ values are observed at $U_r = 2$ and $U_r = 2.5$, for the $G/D = 0.5$ and single cylinder configurations, respectively, and $A_{y,max}/D$ is approximately zero at $U_r = 12$. For the $G/D = 0.5$ configuration, the maximum $A_{y,max}/D$ is approximately $A_{y,max}/D = 1.40$ at $U_r = 8$, which is lower than the peak value observed for the single cylinder configuration of $A_{y,max}/D = 1.52$. The lock-in range for the $G/D = 0.1$ and $G/D = 0.25$ configurations extends beyond $U_r = 12$, where $A_{y,max}/D > 1.0$. This is also observed in the subcritical Reynolds number flow regime studies carried out by Zang and Gao (2014). The maximum observed value of $A_{y,max}/D$ for the $G/D = 0.25$ configuration is approximately $A_{y,max}/D = 1.59$ at $U_r = 6$. Based on the observations made in the present study, G/D has significant influence on the vibration response of the cylinder bundle. For small G/D values ($G/D \leq 0.25$), $A_{y,max}/D$ is increased at high U_r ($U_r > 8$).

4.2.3. Frequency analysis

The frequency spectra of C_L, C_D, y/D and x/D are shown in Figs. 29 and 30 for the $G/D = 0.25$ and $G/D = 0.5$ configurations, respectively. The frequency spectra are presented in the $U_r - fD/U$ plane. In the C_L spectra of $G/D = 0.25$ and $G/D = 0.5$ configurations, the highest amplitudes are observed at low U_r which correspond to the initial branch of VIV. The y/D spectra show peak frequencies in the lock-in regime observed in Fig. 28(a). Overall, the C_D and x/D spectra

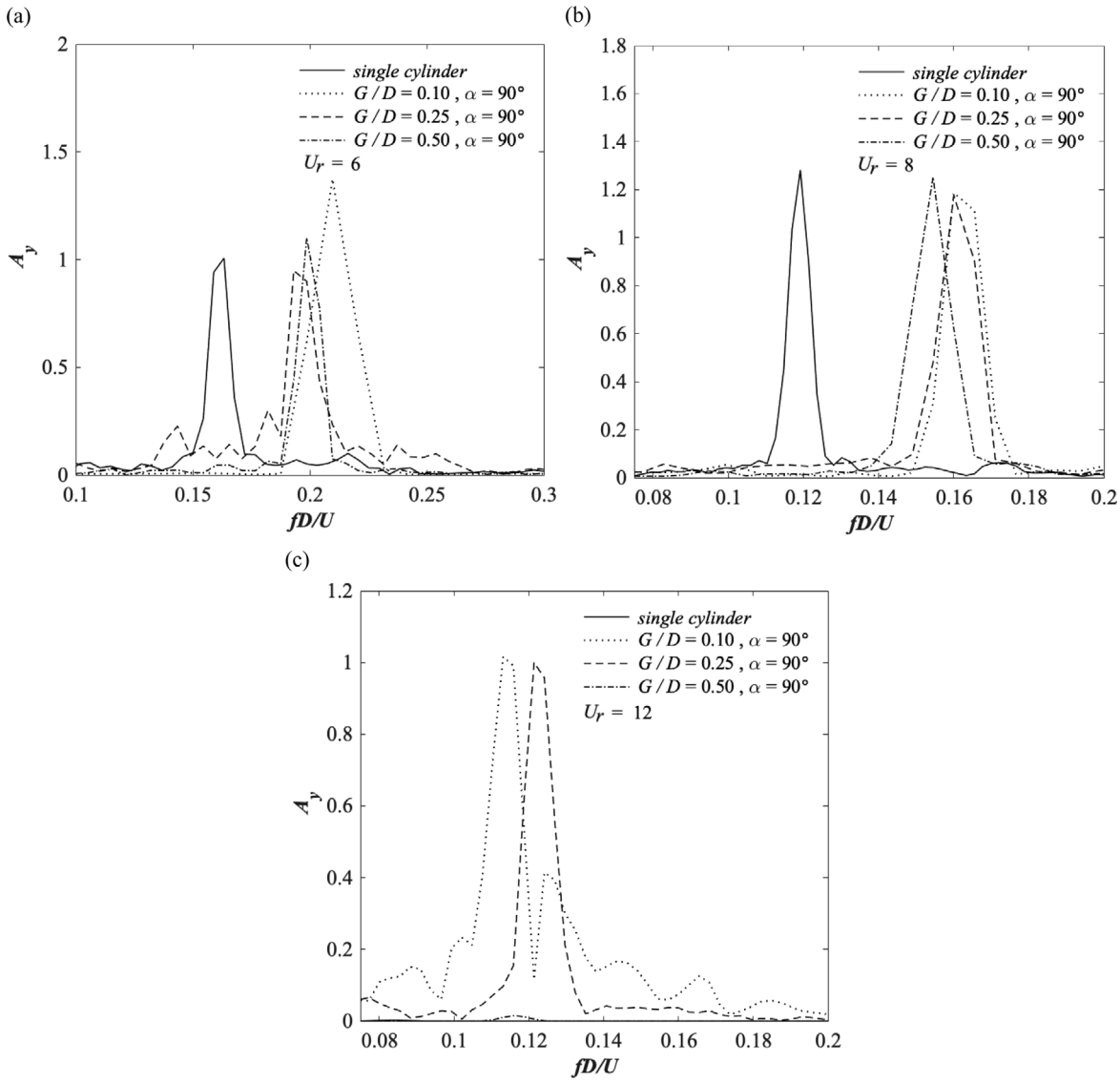

Fig. 31. Frequency spectra of y/D for the single cylinder and $G/D = [0.1, 0.25, 0.5]$ configurations at selected U_r: (a) $U_r = 6$, (b) $U_r = 8$ and (c) $U_r = 12$.

are broadbanded compared with the corresponding spectra of the single cylinder and $G/D = 0.1$ configurations (see Fig. 14).

The frequency spectra of y/D for the single cylinder, $G/D = 0.1$, $G/D = 0.25$ and $G/D = 0.5$ configurations are shown in Fig. 31 for selected U_r cases. They correspond to the cases with the largest transverse amplitude of displacement found in the respective configurations (see Fig. 28(a)). As observed in Rahmanian et al. (2012) for a subcritical Reynolds number flow regime, different dominant frequencies are found for different G/D and the observed maximum values are similar for different G/D. However, it is observed that the effect of G/D on the y/D spectra is smaller compared with the effect of α.

4.2.4. Motion trajectories

Figs. 32 and 33 present the motion trajectories in the x/D–y/D plane for the $G/D = 0.25$ and $G/D = 0.5$ configurations, respectively. The duration of the displacement time series used to plot the motion trajectories is $\tau = 100$. It is observed that the trajectories of $G/D = 0.25$ and $G/D = 0.5$ configurations are narrower compared with those of the $G/D = 0.1$ configuration (see Fig. 20). The in-line motions experienced by $G/D = 0.25$ and $G/D = 0.5$ configurations are smaller compared with those of the $G/D = 0.1$ configuration. The $U_r = 2$ cases of the $G/D = 0.25$ and $G/D = 0.5$ configurations have lower in-line amplitude compared with the $U_r = 2$ case of the single cylinder configuration. Overall, it is seen that

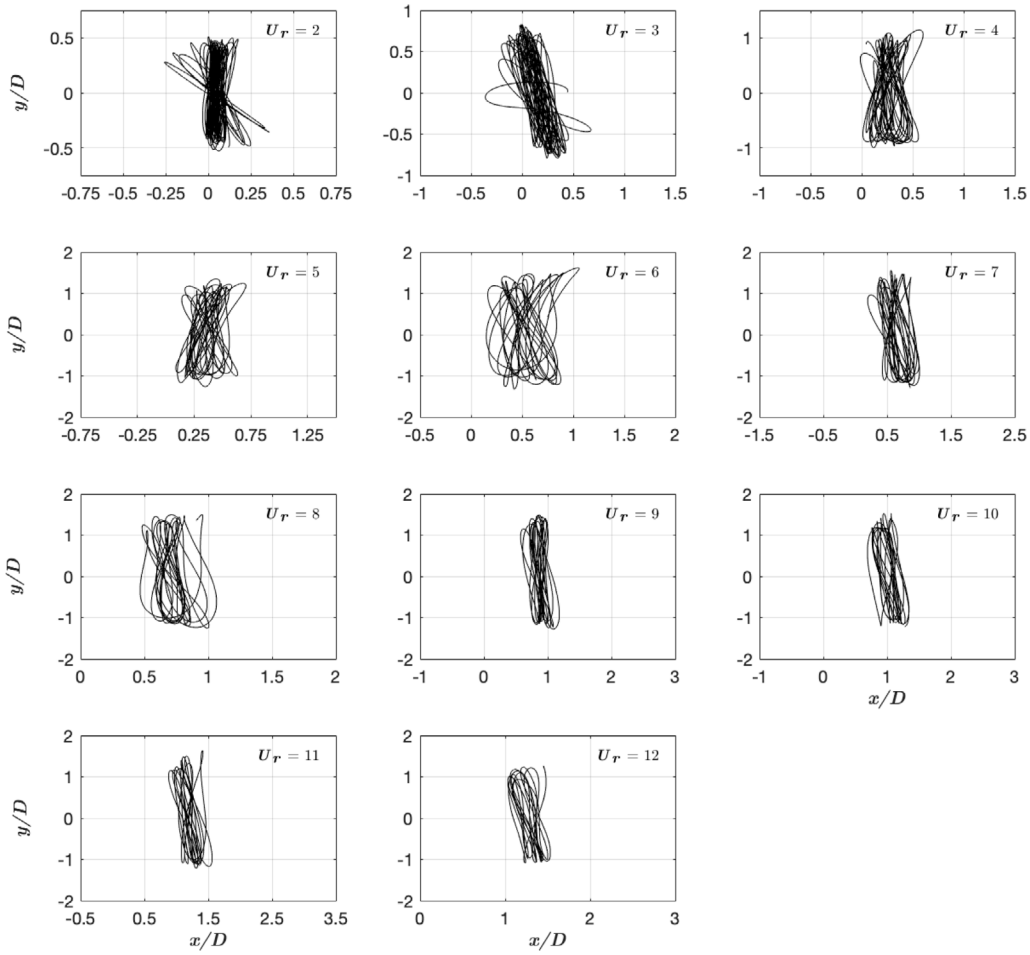

Fig. 32. x/D–y/D trajectory: coupled cylinders $\alpha = 90°$, $G/D = 0.25$.

with increasing G/D, the trajectories converge to those observed for the single cylinder cases (see Fig. 18). This is explained by the decreased influence of the vortex shedding from the small cylinder on the large cylinder with increasing G/D.

4.2.5. Flow field analysis

The flow characteristics around the $G/D = 0.25$ configuration are presented in Fig. 34. When $U_r = 2$, the vortex street from the small cylinder merges with the vortices shed from the top of the large cylinder. In the far wake, the vortex shedding pattern appears to be 2S. For $U_r \geq 5$, the vortex street from the small cylinder breaks the vortices shed on the upper side of the large cylinder. This process results in many vortical structures in the wake of the cylinders.

Fig. 35 shows the flow fields of the $G/D = 0.5$ configuration. It can be observed that with the increase of G/D, the vortex street behind the small cylinder gets longer and affects the vortex shedding from the large cylinder for the whole range of investigated U_r. In general, many vortical structures are generated in the wake of the cylinders and a regular vortex shedding mode is not identified. For $U_r \leq 3$, the near wake is characterized by many small vortices. The vortices shed behind the large cylinder break and merge with the vortex street from the small cylinder. For $4 \leq U_r \leq 11$, the vortex formation length behind the large cylinder is elongated. The shear layers from the large cylinder are attracted by the vortex street from the small cylinder for a longer period of time before shedding. When $U_r = 12$, the structural response is desynchronized from the vortex shedding. The 2S mode is observed behind both the small and large cylinders.

5. Conclusions

In the present study, the flows around a single cylinder and two rigidly coupled cylinders are analyzed at $\mathrm{Re} = 3.6 \times 10^6$. The 2D URANS equations are solved combined with the $k - \omega$ SST turbulence model. Different configurations of the two rigidly coupled cylinders are simulated and their influence on the FIV response of the system is investigated and compared with that of the single cylinder. The numerical model is validated for a stationary single cylinder against the published

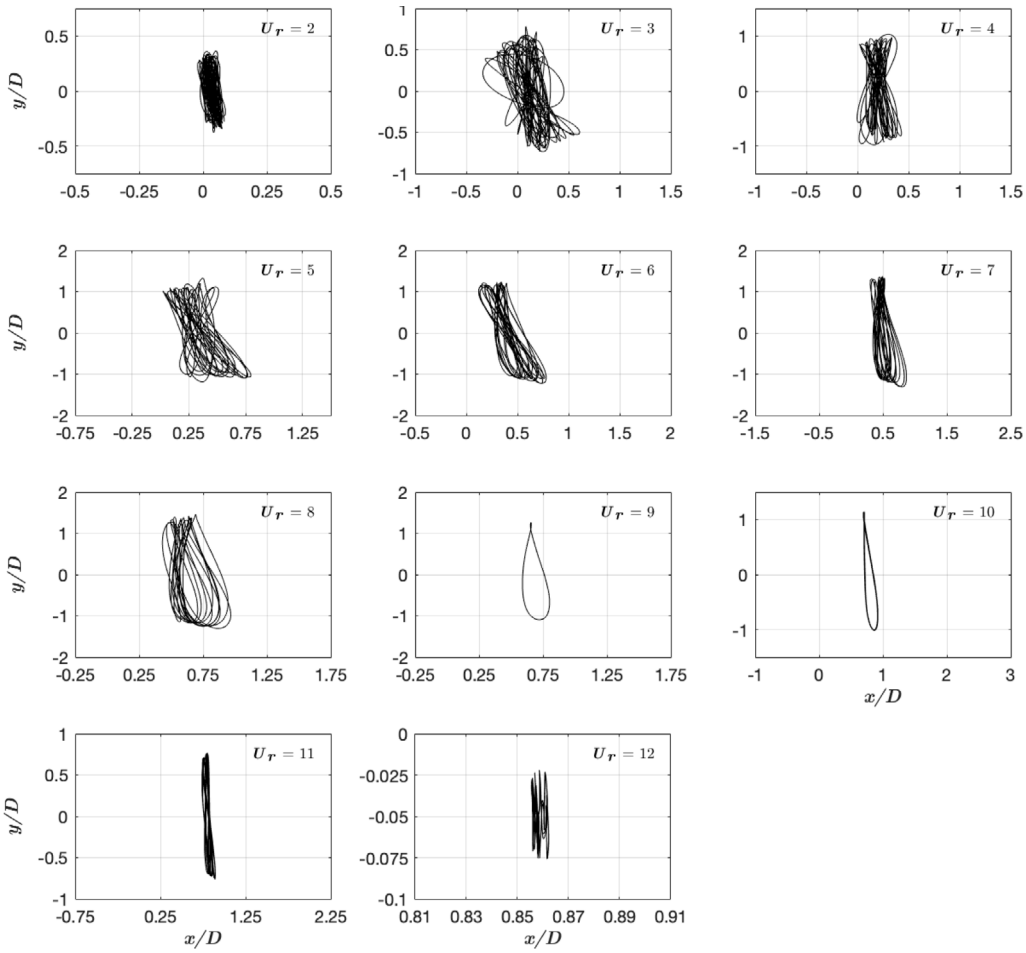

Fig. 33. x/D–y/D trajectory: coupled cylinders $\alpha = 90°$, $G/D = 0.5$.

numerical and experimental studies in the high Reynolds number regime with a satisfactory agreement. The drag and lift coefficients, the in-line and cross-flow vibration amplitudes, the frequency responses, the motion trajectories and the flow fields are discussed. The main conclusions are summarized as follows:

1. Effects of α:

   - In the present study, the highest $\overline{C}_D$ values occur for the $\alpha = 90°$ configuration, and the lowest are observed for the $\alpha = 180°$ configuration. When the cylinders are in tandem with $\alpha = 0°$ and 180°, the results obtained for $\overline{C}_L$ tend to that of the single cylinder, which are found to be around zero. For the $\alpha = 90°$ configuration, the cylinder bundle experiences negative $\overline{C}_L$ for $U_r \leq 3$ and $U_r \geq 11$, and positive $\overline{C}_L$ for $4 \leq U_r \leq 10$.
   - It is found that for the $\alpha = 0°$, $\alpha = 90°$ and $\alpha = 180°$ configurations, the presence of the small cylinder widens the lock-in regime compared with that of the single cylinder. The $\alpha = 0°$ configuration has the lowest $A_{y,max}/D$ value of 1.26, and the highest $A_{y,max}/D$ value of 2.61 is found for the $\alpha = 180°$ configuration. The extended lock-in range is observed for the $\alpha = 90°$ and $\alpha = 180°$ configurations compared to that of the single cylinder.
   - The frequency analysis shows that $\overline{C}_L$ has a peak frequency in the initial branch of FIV for all the configurations. Moreover, the peak frequencies of all the spectra are in the low frequency range of $fD/U < 0.4$ and tend to decrease with the increase of U_r.
   - The $\alpha = 90°$ configuration has irregular motion trajectories, compared with those of the single cylinder, $\alpha = 0°$ and $\alpha = 180°$ configurations.
   - The 2T mode can be clearly seen for the single cylinder configuration at $6.5 \leq U_r \leq 10$ and for the $\alpha = 0°$ configuration when $U_r \geq 8$. The wake patterns observed for the $\alpha = 90°$ and $\alpha = 180°$ configurations are in general, irregular compared with the other configurations.

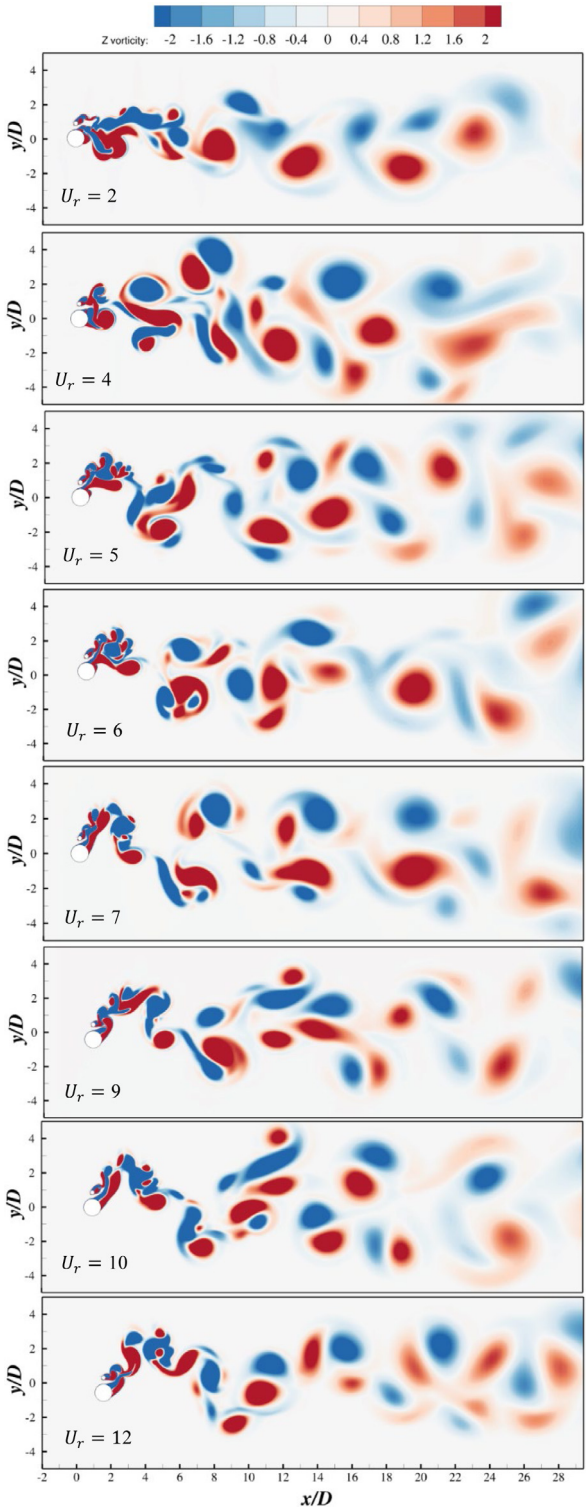

Fig. 34. Vortex shedding patterns at selected U_r: coupled cylinders $\alpha = 90°$, $G/D = 0.25$.

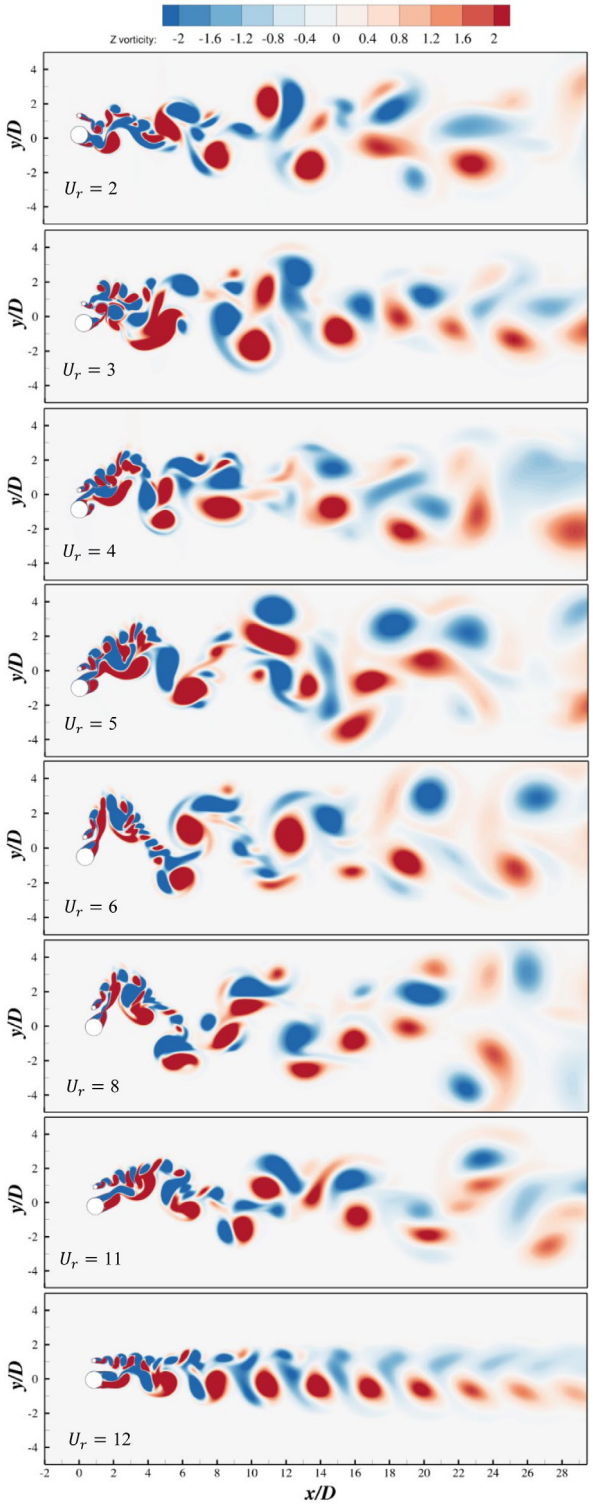

Fig. 35. Vortex shedding patterns at selected U_r: coupled cylinders $\alpha = 90°$, $G/D = 0.5$.

2. Effects of G/D for the $\alpha = 90°$ configuration:

   - It is found that with the increase of G/D, $\overline{C}_D$ values decrease and converge to those observed for the single cylinder. The highest magnitudes of $\overline{C}_L$ are observed for $G/D = 0.1$ and $G/D = 0.25$ configurations. The $\overline{C}_L$ curve for the $G/D = 0.5$ configuration is closer to that of the single cylinder.
   - The lock-in range of the $G/D = 0.5$ configuration is similar to that of the single cylinder. For the $G/D = 0.25$ and $G/D = 0.1$ configurations, the lock-in regime extends beyond $U_r = 12$. The highest $A_{y,max}/D$ value of 1.82 is observed for the $G/D = 0.1$ configuration at $U_r = 12$.
   - The effect of G/D on the FIV response of the cylinder bundle is observed in the motion trajectory. With the increase of G/D, the trajectories become regular and more similar to those observed for the single cylinder.
   - Finally, with the increase of G/D, a longer vortex street behind the small cylinder is observed. This creates many vortical structures in wake of the cylinders and irregular vortex shedding patterns.

CRediT authorship contribution statement

Clarissa Pires Vieira Serta: Conceptualization, Methodology, Software, Validation, Formal analysis, Investigation, Writing - original draft, Writing - review & editing, Visualization. **Marek Jan Janocha:** Conceptualization, Methodology, Software, Investigation, Writing - review & editing, Visualization, Supervision. **Guang Yin:** Conceptualization, Methodology, Software, Investigation, Writing - review & editing, Supervision. **Muk Chen Ong:** Conceptualization, Methodology, Investigation, Resources, Writing - review & editing, Supervision, Project administration, Funding acquisition.

Declaration of competing interest

The authors declare that they have no known competing financial interests or personal relationships that could have appeared to influence the work reported in this paper.

Acknowledgments

This study was supported in part with computational resources provided by the Norwegian Metacenter for Computational Science (NOTUR), Project No. NN9372K. This support is greatly acknowledged.

References

Achenbach, E., 1968. Distribution of local pressure and skin friction around a circular cylinder in cross-flow up to Re = 5×10^6. J. Fluid Mech. 34 (4), 625–639.
Catalano, P., Wang, M., Iaccarino, G., Moin, P., 2003. Numerical simulation of the flow around a circular cylinder at high Reynolds numbers. Int. J. Heat Fluid Flow 24, 463–469.
Feng, C.C., 1968. The measurement of vortex induced effects in flow past stationary and oscillating circular and D-section cylinders. (Ph.D. thesis). University of British Columbia.
Han, X., Lin, W., Wang, D., Qiu, A., Feng, Z., Tang, Y., Wu, J., 2018. Numerical simulation of super upper branch of a cylindrical structure with a low mass ratio. Ocean Eng. 168, 108–120.
Janocha, M.J., Ong, M.C., 2020. Vortex-induced vibrations of piggyback pipelines near the horizontal plane wall in the upper transition regime. Mar. Struct. 75, 1–21.
Jauvtis, N., Williamson, C.H.K., 2004. The effect of two degrees of freedom on vortex-induced vibration at low mass and damping. J. Fluid Mech. 509, 23–62.
Kalghatgi, S.G., Sayer, P.G., 1997. Hydrodynamic forces on piggyback pipeline configurations. J. Waterway Port Coast. Ocean Eng. 123, 16–22.
Kang, Z., Ni, W.-C., Zhang, X., Sun, L., 2017. Two improvements on numerical simulation of 2-dof vortex-induced vibration with low mass ratio. China Ocean Eng. 31 (6), 764–772.
Menter, F.R., Kuntz, M., Langtry, R., 2003. Ten years of industrial experience with the SST turbulence model. Turbul. Heat Mass Transf. 4 (1), 625–632.
Nieto, F., Hargreaves, D.M., Owen, J.S., Hernández, S., 2015. On the applicability of 2D URANS and SST k - ω turbulence model to the fluid–structure interaction of rectangular cylinders. Eng. Appl. Comput. Fluid Mech. 9 (1), 157–173.
Ong, M.C., Utnes, T., Holmedal, L.E., Myrhaug, D., Pettersen, B., 2009. Numerical simulation of flow around a smooth circular cylinder at very high Reynolds numbers. Mar. Struct. 22, 142–153.
Paidoussis, M.P., 2010. Fluid–Structure Interactions: Cross-Flow-Induced Instabilities. Cambridge University Press.
Pang, A.L.J., Skote, M., Lim, S.Y., 2016. Modelling high re flow around a 2D cylindrical bluff body using the k-ω (SST) turbulence model. Prog. Comput. Fluid Dyn. 16 (1), 48–57.
Porteous, A., Habbit, R., Colmenares, J., Poroseva, S., Murman, S.M., 2015. Simulations of incompressible separated turbulent flows around two-dimensional bodies with URANS models in OpenFOAM. In: 22nd AIAA Computational Fluid Dynamics Conference. Dallas, TX.
Rahmanian, M., Zhao, M., Cheng, L., Zhou, T., 2012. Two-degree-of-freedom vortex-induced vibration of two mechanically coupled cylinders of different diameters in steady current. J. Fluids Struct. 35, 133–159.
Roshko, A., 1961. Experiments on the flow past a circular cylinder at very high Reynolds number. J. Fluid Mech. 10 (3), 345–356.
Schmidt, L.V., 1966. Fluctuating force measurements upon a circular cylinder at Reynolds number up to 5×10^6. NASA Technical Report, Document ID 19660022955.
Singh, S.P., Mittal, S., 2005. Flow past a cylinder: shear layer instability and drag crisis. Internat. J. Numer. Methods Fluids 47, 75–98.
Sumer, B.M., Fredsøe, J., 2006. Hydrodynamics Around Cylindrical Structures. Advanced Series on Ocean Engineering, World Scientific Publishing Co. Ptc. Ltd.
Thapa, J., Zhao, M., Cheng, L., Zhou, T., 2015. Three-dimensional flow around two circular cylinders of different diameters in a close proximity. Phys. Fluids 27, 085106-1–085106-16.

Tsutsui, T., Igarashi, T., Kamemoto, K., 1997. Interactive flow around two circular cylinders of different diameters at close proximity. Experiment and numerical analysis by vortex method. J. Wind Eng. Ind. Aerodyn. 69–71, 279–291.

Wu, Wei, Bernitsas, Michael, Maki, Kevin, 2014. RANS Simulation versus experiments of flow induced motion of circular cylinder with passive turbulence control at 35,000 < Re < 130,000. ASME. J. Offshore Mech. Arct. 136 (4), 041802–041812. http://dx.doi.org/10.1115/1.4027895, in press.

Zang, Z.P., Gao, F.P., 2014. Steady current induced vibration of near-bed piggyback pipelines: Configuration effects on VIV suppression. Appl. Ocean Res. 46, 62–69.

Zang, Z., Gao, F., Cui, J., 2012. Vortex shedding and vortex-induced vibration of piggyback pipelines in steady currents. In: The Twenty-Second International Offshore and Polar Engineering Conference. International Society of Offshore and Polar Engineers.

Zang, Z., Gao, F., Mou, Y., Li, Z., 2013. Transverse VIV response of piggyback pipelines with various configurations in ocean current. In: The Twenty-Third International Offshore and Polar Engineering Conference. International Society of Offshore and Polar Engineers.

Zhao, M., Cheng, L., Teng, B., Dong, G., 2007. Hydrodynamic forces on dual cylinders of different diameters in steady currents. J. Fluids Struct. 23, 59–83.

Zhao, M., Cheng, L., Teng, B., Liang, D., 2005. Numerical simulation of viscous flow past two circular cylinders of different diameters. Appl. Ocean Res. 27 (1), 39–55.

Zhao, J., Hourigan, K., Thompson, M.C., 2018. Flow-induced vibration of D-section cylinders: an afterbody is not essential for vortex-induced vibration. J. Fluid Mech. 851, 317–343.

Zhao, J., Leontini, J.S., Lo Jacono, D., Sheridan, J., 2014. Fluid–structure interaction of a square cylinder at different angles of attack. J. Fluid Mech. 747, 688–721.

Zhao, M., Midson, J., Pearcey, T., 2016. Vortex-induced vibration of side-by-side dual cylinders of different diameters. In: The Twelfth ISOPE Pacific/Asia Offshore Mechanics Symposium. International Society of Offshore and Polar Engineers.

Zhao, M., Yan, G., 2013. Numerical simulation of vortex-induced vibration of two circular cylinders of different diameters at low Reynolds number. Phys. Fluids 25 (8), 083601.